Imaging of Single Transducer-Harmonic Motion Imaging-derived Displacements at Several Oscillation Frequencies Simultaneously

Md Murad Hossain, *Member, IEEE*, and Elisa E. Konofagou, *Member, IEEE*

***Abstract*— Mapping of mechanical properties, dependent on the frequency of motion, is relevant in diagnosis, monitoring treatment response, or intra-operative surgical resection planning. While shear wave speeds at different frequencies have been described elsewhere, the effect of frequency on the "on-axis" acoustic radiation force (ARF)-induced displacement has not been previously investigated. Instead of generating single transducer-harmonic motion imaging (ST-HMI)-derived peak-to-peak displacement (P2PD) image at a particular frequency, a novel multi-frequency excitation pulse is proposed to generate P2PD images at 100-1000 Hz simultaneously. The performance of the proposed excitation pulse is compared with the ARFI by imaging 16 different inclusions (Young's moduli of 6, 9, 36, 70 kPa and diameters of 1.6, 2.5, 6.5, and 10.4 mm) embedded in an 18 kPa background. Depending on inclusion size and stiffness, the maximum CNR and contrast were achieved at different frequencies and were always higher than ARFI. The frequency, at which maximum CNR and contrast were achieved, increased with stiffness for fixed inclusion's size and decreased with size for fixed stiffness. *In vivo* feasibility is tested by imaging a 4T1 breast cancer mouse tumor on Day 6, 12, and 19 post-injection of tumor cells. Similar to phantoms, the CNR of ST-HMI images was higher than ARFI and increased with frequency for the tumor on Day 6. Besides, P2PD at 100-1000 Hz indicated that the tumor became stiffer with respect to the neighboring non-cancerous tissue over time. These results indicate the importance of using a multi-frequency excitation pulse to simultaneously generate displacement at multiple frequencies to better delineate inclusions or tumors.**

***Index Terms*— Displacement Imaging; Harmonic motion imaging; ARFI; Ultrasound elastography; Breast Cancer; High-Frequency ARF.**

I. INTRODUCTION

Ultrasound elastography [1], magnetic resonance elastography (MRE) [2], or optical coherence elastography (OCE) [3] derived mechanical properties have been used to diagnose diseases, monitor the efficacy of treatment, and plan surgery [1], [4], [5]. All these elastographic methods are different in terms of the use of the mechanical force to probe the tissue, tracking force-induced deformation, and inferring mechanical properties from the estimated deformation. Due to these differences, the estimated mechanical properties and the perceived size of the lesions/inclusions vary between different elastographic methods [6], [7]. While these variations can be mitigated by assessing mechanical properties as a function of frequency [8], interrogated frequencies are also different among these methods. As an example, MRE uses the single frequency shear wave (i.e., narrowband harmonic shear waves) in the 20-60 Hz range [4] whereas generated shear waves in the ultrasound elastography can be harmonic or transient/impulsive (i.e., broadband frequency range of 50-2000 Hz) [9].

In ultrasound shear wave elastography (SWE), narrowband harmonic shear waves have been generated by an external device [10]–[12] or focused ultrasound transducer (FUS) vibrating continuously at a particular frequency [13] or by repeating a pulsed ARF at a particular frequency [14] or modulating ARF excitation pulse duration [15], [16]. Rather than generating narrowband harmonic shear waves, impulsive ARF was also used to generate shear waves in the wide frequency range and shear wave at a particular frequency (i.e., phase velocity) was calculated in the frequency domain using phase gradients or Fourier transform methods [17]–[22]. While these methods were mainly used to study phase velocity dispersion due to viscoelasticity [17]–[22] and geometry of the ARF [23], the selection of frequencies is important to correctly estimate mechanical properties and detect inclusion. Higher frequencies are better suited to reconstruct the shape of the stiffer inclusions and detect smaller inclusions with isotropic mechanical properties [20] and estimate fiber orientation and shear wave speed in anisotropic materials [24]. However, shear waves with higher frequencies attenuate more and do not propagate further from the source [25].

In contrast to the shear wave-based measurements, some ARF-based elastographic methods used displacements "on-axis" to the ARF to estimate mechanical properties of tissue [26]–[29]. Though "on-axis" ARF based methods provide qualitative mechanical properties compared to the quantitative values provided by the SWE, "on-axis" methods may provide better mechanical resolution [30], be less distorted by tissue heterogeneity, reflected waves, and anisotropy [31], and provide higher penetration depth [32] compared to the SWE. Some "on-axis" ARF- based methods include acoustic radiation force impulse (ARFI) imaging [26], ARF creep imaging [33], viscoelastic response (VisR) ultrasound imaging [29], [34], kinetic acoustic vitreoretial examination (KAVE) [35], Vibro-acoustography (VA) [36] and harmonic motion imaging (HMI) [28]. The "on-axis" methods, other than HMI or VA, used single [26] or several impulsive ARF excitation pulses co-localized in space-separated in time [29], [33]–[35] to assess mechanical properties of tissues. In VA [36], [37], or HMI [28], ARF is used to continuously oscillate tissue at a particular frequency. Due to the known frequency, the VA or HMI-derived mechanical properties are robust against artifacts due to the reverberation, movement, and breathing. While the HMI has been used for detecting pancreatic tumors [38], monitoring treatment response of pancreatic tumors [39], monitoring high intensity focused ultrasound-induced ablation of tumors [40], [41], and livers [42], the current use of two different transducers with a mechanical positioner to generate a 2-D image renders the HMI system highly complex to use for diagnostic imaging.

To facilitate HMI data acquisitions while preserving the

Manuscript submitted March 16, 2022. This work was supported by NIH under Grant R01 CA228275 (Corresponding author: Md Murad Hossain). M. M. Hossain and E. E. Konofagou are with the Department of Biomedical Engineering, Columbia University, New York, NY 10027 USA. (mh4051@columbia.edu).

advantages of the amplitude modulated (AM) ARF-induced harmonic excitation, Hossain *et al.* proposed a single transducer –HMI (ST-HMI) to generate and map narrowband harmonic motion using an imaging transducer [43], [44]. In ST-HMI, the AM-ARF is generated by modulating the excitation pulse duration and the AM-ARF-induced motion is tracked by transmitting the tracking pulses in between the discrete excitation pulses. Note, changes in the excitation pulse duration change the integrated intensity of the pulse which in turn generates different magnitude ARF [26]. While the shear wave or phase velocity as a function of frequency was well investigated in the past, the impact of frequency on the "on-axis" displacement was not studied extensively. By varying ST-HMI oscillation frequency from 60 – 420 Hz, Hossain *et al.* showed that the oscillation frequency could be exploited to improve the contrast-to-noise ratio (CNR) of 15 and 60 kPa inclusions [43]. However, the effect of oscillation frequency in detecting different size inclusion was not studied previously. The main limitation of [43] was the separate acquisition of each frequency data from 60 to 420 Hz. This may be unrealistic in a clinical imaging scenario due to the long imaging time and difficulty in registering different frequency images if there are patients' or sonographers' hand movements during the separate collection of several frequencies. Instead of collecting each frequency separately, the more realistic option is to collect several frequencies simultaneously.

Towards the goal of generating ST-HMI-derived motion at several frequencies simultaneously, this study investigates the use of a new multi-frequency excitation pulse which is composed of a sum of sinusoids with desired frequencies. Similar to [43], the continuous multi-frequency excitation pulse is sampled and the tracking pulses are transmitted in between the discrete excitation pulses. The estimated displacements are filtered out to generate peak-to-peak displacements (P2PD) at corresponding frequencies of the multi-frequency excitation pulse.

The objectives of this study are as follows. First, the feasibility of generating P2PD images at 100-1000 Hz frequencies is demonstrated using an excitation pulse composed of a sum of sinusoids with the corresponding frequencies and higher weights to the larger frequencies. To the best of our knowledge, no previous studies investigated "on-axis" displacement at these high frequencies. Second, the impact of inclusion size and stiffness on the contrast and CNR derived at 100-1000 Hz frequencies is investigated by imaging different inclusion sizes (N = 4) and stiffnesses (N=4). Third, the advantages of exploiting oscillation frequencies over ARFI-derived peak displacement (PD) are demonstrated. Note that, ARFI uses impulsive ARF to generate displacements with a wide frequency range. Fourth, the *in vivo* feasibility of generating P2PD images at 100-1000 Hz frequencies is demonstrated by imaging tumors in a 4T1 breast cancer mouse model.

II. Materials and Methods

A. Excitation Pulse Composed of Sum of Sinusoids

The proposed multi-frequency excitation pulse was composed of a sum of sinusoids with the lowest frequency of f_L and was generated as follows:

$$e_1(t) = \sum_{j=1}^{N_{sinusoid}} j^2 \times cos(2\pi j f_L t + \theta_j) \qquad (1)$$
$$where,\ \theta_j = \begin{cases} \pi, & if\ j\ odd \\ 0, & if\ j\ even \end{cases}$$

where $N_{sinusoid}$ defines the total number of sinusoids with a frequency of an integer multiple of the lowest frequency of f_L. Therefore, the maximum frequency in $e_1(t)$ is $N_{sinusoid} \times f_L$. The duration of the continuous excitation pulse is the product of the total cycle number (N_{cycle}) and fundamental period of f_L (i.e., $1/f_L$). For example, if a continuous excitation pulse contains 6 cycles of f_L = 100 Hz (i.e, fundamental period = 1000/100 ms), the duration of continuous excitation pulse will be 6*1000/100 ms = 60 ms. The multiplication term, j^2 , in (1) is added to account for the higher loss in the higher frequencies. The phase (θj) of sinusoids alternates between 0 and π to maximize the $e_1(t)$ dynamic range by constructively (5 ms) or destructively (4.5 and 5.7 ms) summing sinusoids at different time points, which will produce motion at a wider dynamic range because pulse intensity (or ARF magnitude) is directly proportional to the pulse duration. As $e_1(t)$ is generated by adding sinusoids, $e_1(t)$ contains both positive and negative values. However, the excitation pulse duration can not be negative. Therefore, a dc offset, A_{offset}, is added to $e_1(t)$ as follows:

$$e_2(t) = A_{offset} + e_1(t) \qquad (2)$$
$$where,\ A_{offset} = -A_{factor} \times \min(e_1(t))$$

where, $min(e_1(t))$ means minimum of $e_1(t)$. A_{factor} in (2) defines the minimum continuous excitation pulse duration. Therefore, A_{factor} has to be greater than 1.0 to have only positive values in $e_2(t)$. Note, A_{factor} sets to 1.25 for all experiments (see Table I). While the A_{offset} is determined from the pulse duration, it does not need to depend on the $e_1(t)$. Any dc values can be added to have only positive values in the continuous pulse. Finally, $e_2(t)$ is normalized as follows to have a maximum excitation pulse duration of t_{ARF}^{max}.

$$e(t) = \frac{t_{ARF}^{max} \times e_2(t)}{max(e_2(t))} \qquad (3)$$

where, $max(e_2(t))$ means maximum of $e_2(t)$. However, $e(t)$ in (3) is a continuous excitation pulse (see Fig. 2a). After setting A_{factor} = 1.25 and t_{ARF}^{max} = 100 µs, minimum continuous excitation pulse became 10 µs (see Fig. 2a). To accommodate both discrete excitation and tracking pulses, $e(t)$ is sampled to generate N_{ep} discrete excitation pulses as follows:

$$E[n] = e(t) \times \sum_{n=1}^{N_{ep}} \delta(t - t_n) \qquad (4)$$

where δ is the Delta-Dirac function and t_n defines the nth discrete excitation pulse's location in the time-axis. Tracking pulses are interleaved with N_{ep} discrete excitation pulses (see Fig. 2b). The induced displacement was estimated relative to the reference tracking pulse which was transmitted at the start of excitation and tracking pulse sequence.

B. In Silico Model

The *in silico* model consists of Field II [45], [46] and LS-DYNA3D (Livermore Software Technology Corp. Livermore,

CA), a finite element method (FEM) solver. The model was adapted from [47]–[49] to simulate multi-frequency ST-HMI and ARFI imaging of elastic solid with parameters in Table I. The axial, lateral, and elevational range of the FEM mesh was 5 to 42 mm, −8 to 8 mm, and −6 to 6 mm, respectively with an isotropic element size of 0.2 x 0.2 x 0.2 mm^3. A 2 mm diameter spherical inclusion was embedded in the background with the center (elevational, lateral, axial) of the inclusion at (0, 0, 30) mm. The Young's moduli of the background and inclusion were set to 18 and 22.5 kPa, respectively with the Poisson's ratio of 0.499.

To simulate ultrasonic tracking of displacements, scatterers in Field II were moved according to the FEM displacement estimates with the parameters in Table I. Eleven independent unique scatter realizations with 15 scatterers per resolution cell were implemented. White Gaussian noise was added Field II generated RF data using the *awgn* function in MATLAB (Mathworks Inc., Natick, MA, USA) to simulate system echo SNR of 25 dB. Motion tracking was performed by one-dimensional axial normalized cross-correlation (NCC) using the parameters listed in Table I [50]. The focal depth of the excitation and tracking pulse was at 30 mm and a 2-D image was generated by moving the lateral focus location from -4 to 4 mm in steps of 0.4 mm.

C. Phantom Experiments

The feasibility of generating displacements at multi-frequencies simultaneously was tested by imaging a commercially available elastic phantom (model 049A, Computerized Imaging Reference Systems (CIRS) Inc, Norfolk, VA, USA). The imaging was performed using a Verasonics research system (Vantage 256, Verasonics Inc., Kirkland, WA, USA) equipped with an L7-4 transducer (Philips Healthcare, Andover, MA, USA). Using a clamp, the transducer was held in a steady position. Four stepped-cylindrical inclusions with nominal Young's moduli of 6, 9, 36, and 70 kPa were embedded in the background with nominal Young's modulus of 18 kPa. For each stiffness, imaging was performed at cross-sections with 1.6, 2.5, 6.5, and 10.4 mm diameters. The manufacturer provided standard deviation in elasticity and diameters measurements was approximately 5%. The center of the inclusion was approximately 30 mm from the phantom's surface. However, water was added between the transducer's and phantom's surface which resulted in the center of inclusion at 34 mm from the transducer surface. Throughout the remainder of the manuscript, each inclusion will be represented by its mean nominal Young's modulus and diameter.

The performance of ST-HMI with multi-frequency excitation pulse was compared to ARFI imaging [26]. The ARFI and ST-HMI imaging were performed consecutively using the methods described in [26], [43], [51] with parameters indicated in Table I. Briefly, both ARFI and ST-HMI data were collected using focused excitation and tracking beams generated with sub-aperture and translated electronically across the lateral field to generate a 2-D image. Thirty-two or Thirty-eight evenly spaced RF lines with 0.6 mm or 0.3 mm spacing between RF lines were acquired to image inclusions with diameters of (10.4 and 6.5 mm) or (2.5 and 1.6 mm), respectively. Wiper blading scanning mode [52] was used to prevent interference in the tissue mechanical response between consecutive RF lines and reduce transducer face heating. One frame of the B-mode ultrasound image with 128 RF lines spanning approximately 38 mm in lateral direction was collected preceding ARFI and ST-HMI imaging. By moving the transducer in the elevational direction, six repeated acquisitions of ARFI and ST-HMI were acquired at each inclusion stiffness and size. The acquisition time of (ST-HMI, ARFI) data with 32 RF lines took approximately (6, 4) s with (0.1, 0.08) s interval between RF lines.

Table I
EXCITATION AND TRACKING PARAMETERS OF ACOUSTIC RADIATION FORCE IMPULSE (ARFI) USED IN IMAGING PHANTOMS AND SINGLE TRANSDUCER-HARMONIC MOTION IMAGING (ST-HMI) USED IN IMAGING PHANTOMS AND BREAST CANCER MOUSE TUMOR WITH NORMALIZED CROSS CORRELATION PARAMETERS FOR DISPLACEMENT ESTIMATION.

Parameters	Phantom (Simulation)	Mouse
Beam sequence parameters of ST-HMI / ARFI		
Transducer	L7-4	L11-5
Bandwidth	58%	77%
Sampling frequency	20.84 MHz	31.3 MHz
Acoustic lens axial focus	25 mm	18 mm
Excitation pulse center frequency	4.0 MHz	5.0 MHz
Excitation pulse F-number	2.25	2.25
Tracking pulse center frequency	6.1 MHz	8.0 MHz
Tracking pulse transmit F-number	1.75	1.75
Tracking pulse receive F-number*	1.0	1.0
Excitation and tracking pulse axial focus	34 (30) mm	22 mm
Spacing between RF-lines	0.59 / 0.3 (0.2) mm	0.6 / 0.3 mm
RF-lines number/image	32 / 38 (16)	30
Lateral field of view size	20 / 11 (8) mm	18 / 9 mm
Tracking pulse PRF	10 KHz	12 KHz
ST-HMI specific parameters		
Lowest oscillation frequency, f_L	100 Hz	100 Hz
Sinusoids number, $N_{sinusoid}$	10	10
A_{factor}	1.25	1.25
Maximum excitation pulse duration, t_{ARF}^{max}	100 µs	40 µs
Discrete excitation pulse duration range	35 - 100 µs	45 - 60 µs
Discrete excitation pulse per f_L	6	7
Cycle number, N_{cycle}	6 (4)	4
ARFI Specific parameters		
Tracking pulse number	110 (30)	130
Excitation pulse duration	113 µs	75 µs
Normalized cross correlation parameter		
Interpolation factor	4	4
Kernel length	592 µm	492 µm
Search region	80 µm	80 µm

* Aperture growth and dynamic Rx focusing enabled

D. Imaging of A breast cancer mouse model, In Vivo

The *in vivo* performance of the proposed excitation pulse sequence was investigated by imaging tumors in an orthotropic, 4T1 breast cancer mouse model (N=1). The Columbia University Irving Medical Center (CUIMC) Institutional Animal

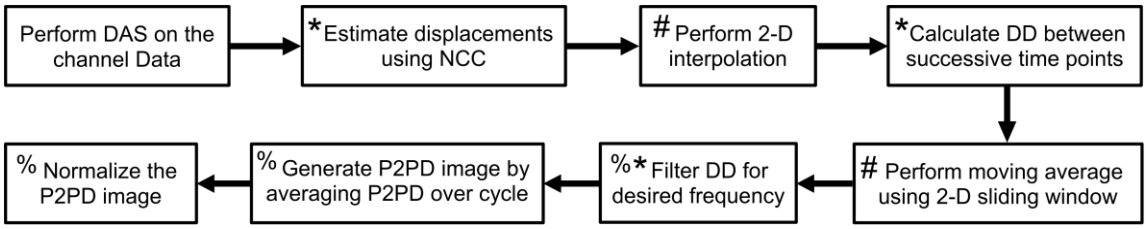

Fig 1: Data processing steps employed to generate ST-HMI-derived peak-2-peak displacement (P2PD) image at each frequency. Steps marked by *, #, and % mean steps are repeated for each pixel, time point, and frequency, repectivey. Note, some steps are repated for more than one cases. DAS = Dealy-and-sum; NCC = Normalized cross-correlation; DD = Differential displacments;

Care and Use Committee (IACUC) reviewed and approved the protocol for the cancer induction and imaging of the mouse's tumors. Tumors were generated by injecting 1 x 10^5 4T1 breast cancer cells in the 4th inguinal mammary fat pad of the eight to ten-week-old female BALB/c mice (Jackson Laboratory)[53], [54].

The same Vantage Verasonics research system equipped with an L11-5 (Verasonics) linear array was used to perform ST-HMI and ARFI with the setup described in [43]. Briefly, the anesthetized mice (1- 2% isoflurane in oxygen) were imaged by placing the mice in a supine position on a heating pad with their abdominal hair removed, and the transducer was held in a steady position using a clamp during imaging. The mouse was imaged on Day 6, 12, and 19 post-injection of cancer cells using the parameters indicated in Table I. Thirty evenly spaced RF-lines with 0.3 or 0.6 mm separation in between RF-lines were acquired to generate 2-D images of ST-HMI-derived P2PDs. Preceding each ST-HMI sequence, one spatially-matched B-mode image was acquired with 128 lateral lines spanning approximately 38 mm, for anatomical reference.

E. ST-HMI and ARFI Data Processing

The channel data were stored onto the Verasonics workstation after running ARFI and ST-HMI imaging sequence and were transferred to the computational workstation for offline processing using MATLAB (MathWorks Inc., Natick, MA, USA). A custom delay-and-sum beamforming [55] was applied to the channel data to construct beamformed radiofrequency (RF) data. 1-D NCC [50] (Table I) was applied to estimate displacement relative to the reference tracking pulse which yielded in a 3-D dataset (axial x lateral x time) describing axial displacements over time.

From the ARFI 3-D dataset, a parametric 2-D image of PD was generated after applying a linear filter [56] to the displacement versus time profile at each pixel [43]. Finally, ARFI-derived PD images were normalized to account for the variation in the ARF magnitude over the axial range [57]. A 2-D spline interpolation (*interp2* function) was applied to the normalized PD image to convert the anisotropic pixel dimension (0.04 x 0.6 mm or 0.04 x 0.3 mm) to an isotropic pixel dimension of 0.1 mm.

2-D parametric image of ST-HMI-derived P2PD at each frequency was generated using the method described in [43] as follows. First, a 2-D spline interpolation (*interp2* function) was applied to the 2-D displacement data at each time point to convert the anisotropic pixel size to an isotropic pixel size of 0.1 mm. Second, the differential displacements at each pixel were computed by subtracting displacements between successive time points to remove the slowly varying motion. Third, the differential displacements at each time point were averaged using a 2-D sliding window with a 0.8 x 0.8 mm kernel. Note, the differential displacements calculation can act as a high pass filter and has the potential to enhance noise. Therefore, the spatial averaging of the differential displacements was performed to reduce noise before filtering out displacement at each frequency. Fourth, the differential displacement profiles were filtered out using a fourth-order infinite impulse response (IIR) bandpass filter (*designfilt* and *filter* function) to estimate displacements at each frequency. It is noteworthy to mention that filtering of differential displacement profiles was performed separately at each frequency. At each pixel, the cutoff values of the bandpass filter were selected adaptively [43]. Fifth, the filtered displacement profile at each pixel and each frequency were integrated (*cumsum* function in MATLAB) and normalized to a zero mean. Sixth, using the integrated-filtered displacement profile, the average P2PD over cycle was calculated at each pixel, and then, rendered into a 2-D parametric image. Note, The number of cycles varies between frequencies as the duration of the continuous excitation pulse was fixed. As an example, if the duration of the continuous excitation pulse is 60 ms with f_L = 100 Hz, then 100 and 1000 Hz had 6 cycles and 60 cycles of oscillation, respectively (Table I). Seventh, P2PD images at each frequency were normalized separately to account for the variation in the ARF magnitude over the axial range [43]. The normalizing profiles for both ARFI and ST-HMI were generated from the 1.5 mm leftmost and rightmost lateral field of view (FOV) [43]. Fig. 1 depicts a flowchart representing the processing steps implemented to generate normalized P2PD images at each frequency.

It took 5 min to process data from performing the delay-and-sum beamforming to generating the final normalized P2PD image at each frequency using a 2.2 GHz Intel Xeon Platinum processor with a 20 cores processor. The computational time can be reduced by implementing ST-HMI data processing pipelines (Fig. 1) in CUDA GPU.

F. Image Quality Metrics

The performance of ARFI-derived PD and ST-HMI-derived P2PD images were compared quantitatively in terms of contrast and CNR with the region of interests (ROIs) in inclusion (INC) and background (BKD) as the concentric circle and ring, respectively (see Fig. 3a) [43]. The inclusion's ROI was defined as the concentric circle with 80% of the corresponding inclusion's radius. The background ROI was defined as a ring surrounding the inclusion, with an inner radius of 120% of the corresponding inclusion' radius. Contrast and CNR were

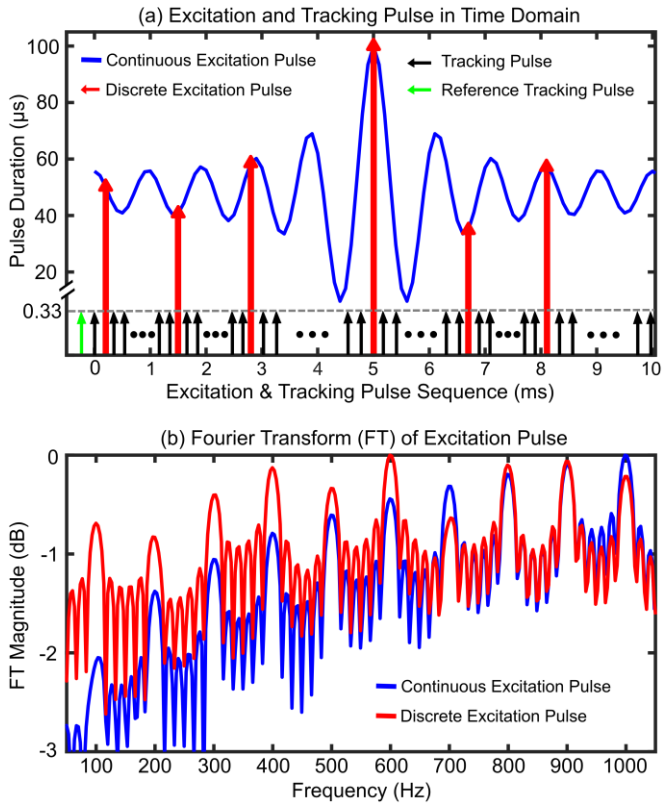

Fig 2: (a) Tracking pulses (black arrow) interleaved with discrete excitation pulses (red arrow) after sampling a continuous excitation pulse (blue). Displacement was estimated with respect to the reference tracking pulse (green arrow). Y-axis contains a break to accommodate the difference in excitation and tracking pulse duration. (b) Fourier transform (FT) magnitude spectra of continuous (blue) and discrete (red) excitation pulse. FT was calcuated using 6 cycles of respective excitation pulse i.e after repeating continuous and discrete pulse in panel (a) 6 times with mean normalized to zero .

computed as $|\mu_{INC} - \mu_{BKD}| / \mu_{BKD}$ and $|\mu_{INC} - \mu_{BKD}| / \sqrt{(\sigma_{INC}^2 + \sigma_{BKD}^2)}$, respectively, where, μ and σ are the median and standard deviation of normalized displacements in the ROI.

To perform linear regression between P2PD ratios versus Young's moduli ratios, a rectangular ROI (see Fig. 3a) [43] was used to avoid the boundary effects. The inclusion's boundary was derived from the B-mode image (see Figs. 3a and 6).

G. Statistical Analysis

All statistical analyses were performed in MATLAB. Thirty-two (diameter, N = 4, stiffness, N = 4) separate Kruskal-Wallis tests (*kruskalwallis* function), were carried out to compare the contrast and CNR of ARFI-derived PD and ST-HMI derived P2PD images at 100-1000 Hz. If any group was statistically significant, a two-sample Wilcoxon signed rank-sum test (*signrank* function) was used to find which combination was statistically significant. The R^2, slope, and root mean square error (RMSE) of the linear regression between the PD or P2PD ratio versus Young's moduli ratio was calculated at each frequency and inclusion size. The RMSE was calculated between displacement ratio (DR) and Young's Moduli ratio. For all the analyses, the statistical significance was based on $p < 0.05$.

III. Results

Fig. 2(a) shows multi-frequency continuous excitation pulse, *e(t)* (equation (3)) with $N_{sinusoid} = 10$, $N_{cycle} = 1$, and $f_L = 100$ Hz. From here onward, 100:100:1000 Hz will represent frequencies from 100 to 1000 Hz in steps of 100 Hz. Therefore, the continuous excitation pulse mainly contains frequencies from 100 to 1000 Hz in steps of 100 Hz. While 1 cycle of excitation pulse is shown in Fig. 2, data were collected using 6 (phantom) or 4 (mouse) cycles of $f_L = 100$ Hz (Table I) i.e total duration of excitation pulse was 60 ms (phantom) or 40 ms (mouse). The Y-axis in Fig. 2a is shown in terms of the pulse duration to underline the change in pulse duration over time because the ST-HMI modulates the excitation pulse duration to generate amplitude modulated-ARF (AM-ARF). The continuous excitation pulse was sampled to accommodate both tracking (black) and discrete excitation (red) pulses. Note, there were only 6 discrete excitation pulses ($N_{ep} = 6$) per one period of 100

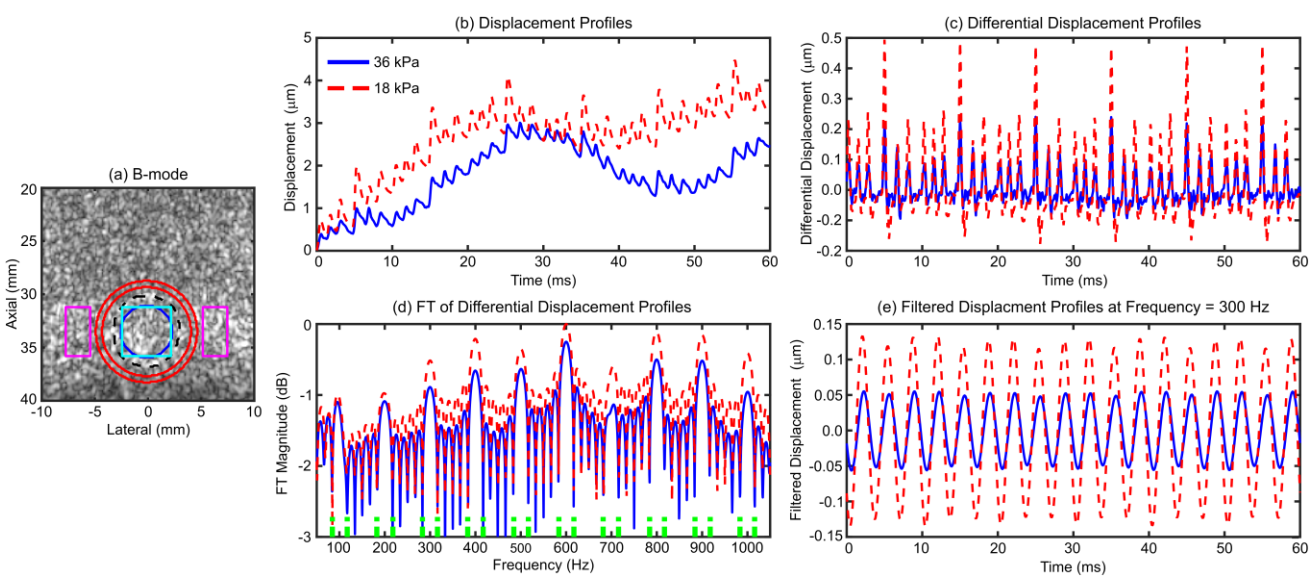

Fig 3: (a) B-mode ultrasound image of 6.5 mm, 36 kPa inclusion. Inclusion boundary (black dashed circle) was derived from the B-mode image and used to draw region of interests (circle or ring or rectange) in inclusion and background. ST-HMI derived (b) displacement profiles (c) differential displacement between successive time points (d) magnitude spectrum of Fourier transform (FT) of the differential displacement profiles (e) filtered displacement profiles at 300 Hz in 36 kPa inclusion (blue) and 18 kPa background (red). Green dahsed lines in panel (d) represent adaptively selected cutoff values for the bandpass filter.

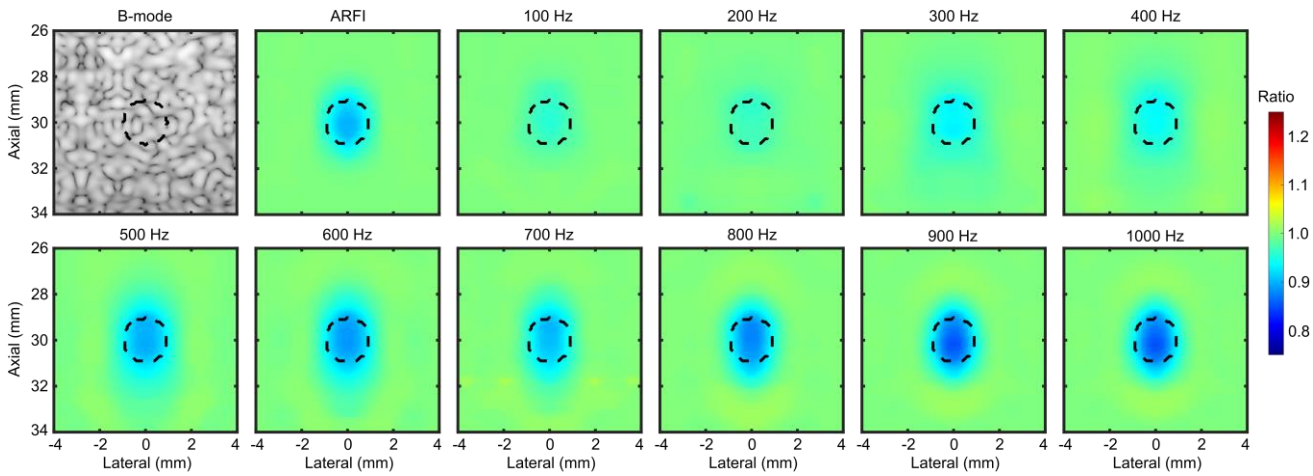

Fig 4: Simulated phantom: Bmode, normalized ARFI peak displacement, and ST-HMI derived normalized peak-to-peak displacement images at 100- 1000 Hz of a 22.5 kPa inclusion with 2 mm diameter embedded in 18 kPa background. Black contour represents the true inclusion boundary.

Hz (i.e, 10 ms). The duration of the discrete excitation pulses was variable (35-100 µs) but the tracking pulse duration was fixed to 0.33 µs (i.e., 2 cycles of 6 MHz). The number of the tracking pulses in between the excitation pulses depends on the pulse repetition frequency (PRF) of the tracking pulse (Table I). Fig. 2(b) shows Fourier transform (FT) magnitude spectra of continuous (blue) and discrete (red) excitation pulse. Both spectra contain 10 peaks at 100 to 1000 Hz in steps of 100 Hz with maximum magnitude at 600 and 1000 Hz for discrete and continuous excitation pulse, respectively.

Fig. 3 shows a representative B-mode ultrasound image of a 6.5 mm, 36 kPa inclusion embedded in an 18 kPa background (panel (a)) and representative displacement profiles in inclusion and background with frequency spectrum (panels (b)-(e)). The inclusion's boundary was derived from the B-mode and was used to draw ROI for contrast and CNR calculation (section II.E). Displacements (panel (b)) or differential displacements (panel (c)) were higher in 18 kPa versus 36 kPa material which is expected. Six peaks per period (10 ms) correspond to the six discrete excitation pulses (Fig. 2a). The amplitude of each peak was different due to the difference in the duration of the discrete excitation pulse. The Fourier transform of the differential displacements (panel (d)) contains peaks at 100:100:1000 Hz. These indicate that the multi-frequency excitation pulse with peaks at 100:100:1000 Hz generated displacements with peaks at 100:100:1000 Hz. Panel (e) shows displacements at 300 Hz after applying Bandpass filtering with [283 315] Hz cutoff values to the differential displacement profiles. The P2PD was 0.11 and 0.27 µm in 36 and 18 kPa materials at 300 Hz. Similar to panel (e), P2PDs were calculated for each pixel and each frequency to generate P2PD images at corresponding frequencies.

Fig. 4 shows B-mode, ARFI normalized PD, and ST-HMI normalized P2PD images at 100-1000 Hz of a 22.5 kPa, 2 mm diameter simulated spherical inclusion embedded in an 18 kPa background. These images were generated by averaging 11 independent speckle realizations. Despite the lower difference in Young's moduli in inclusion versus background, both PD and P2PD at greater than 400 Hz detected the presence of inclusion. However, the perceived contrast and boundary delineation were better at 800-1000 Hz than the PD image. Throughout the manuscript, detecting an inclusion will refer to qualitative comparison when the inclusion pixel values are clearly different than the background pixel values. The qualitative results are confirmed by the CNR and contrast results which are shown in

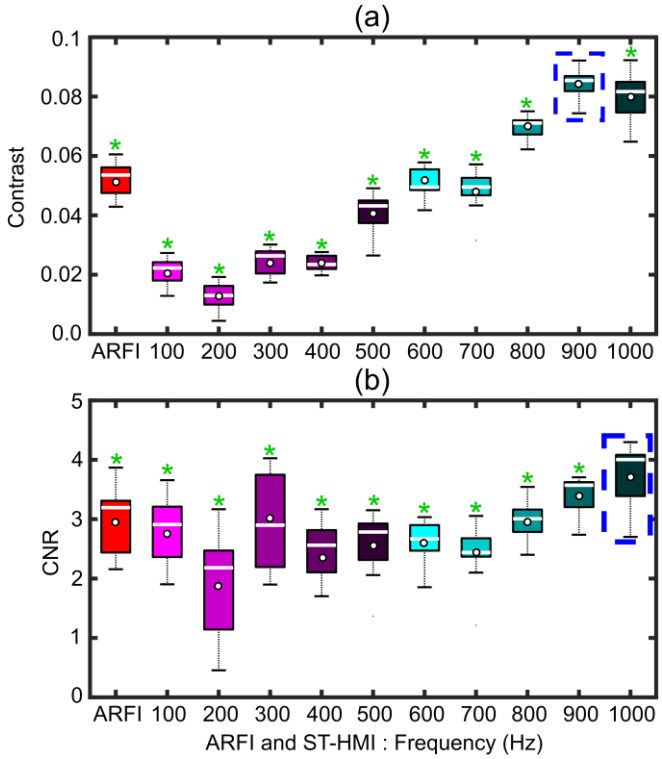

Fig 5: Simulated phantom: (a) Contrast and (b) CNR of ARFI and ST-HMI derived images at 100-1000 Hz of 2 mm, 22.5 kPa inclusion embedded in 18 kPa background. Data are plotted as median ± 0.5*interquartile range over 11 independent speckle realizations. The Kruskal–Wallis test suggested that contrast and CNR were statistically different across ARFI and ST-HMI. For clarity, the asterisk is only shown when Kruskal–Wallis test suggests a statistical difference and median contrast and CNR were statistically different (sign ranksum) from the highest median contrast and CNR (dotted blue rectangle).

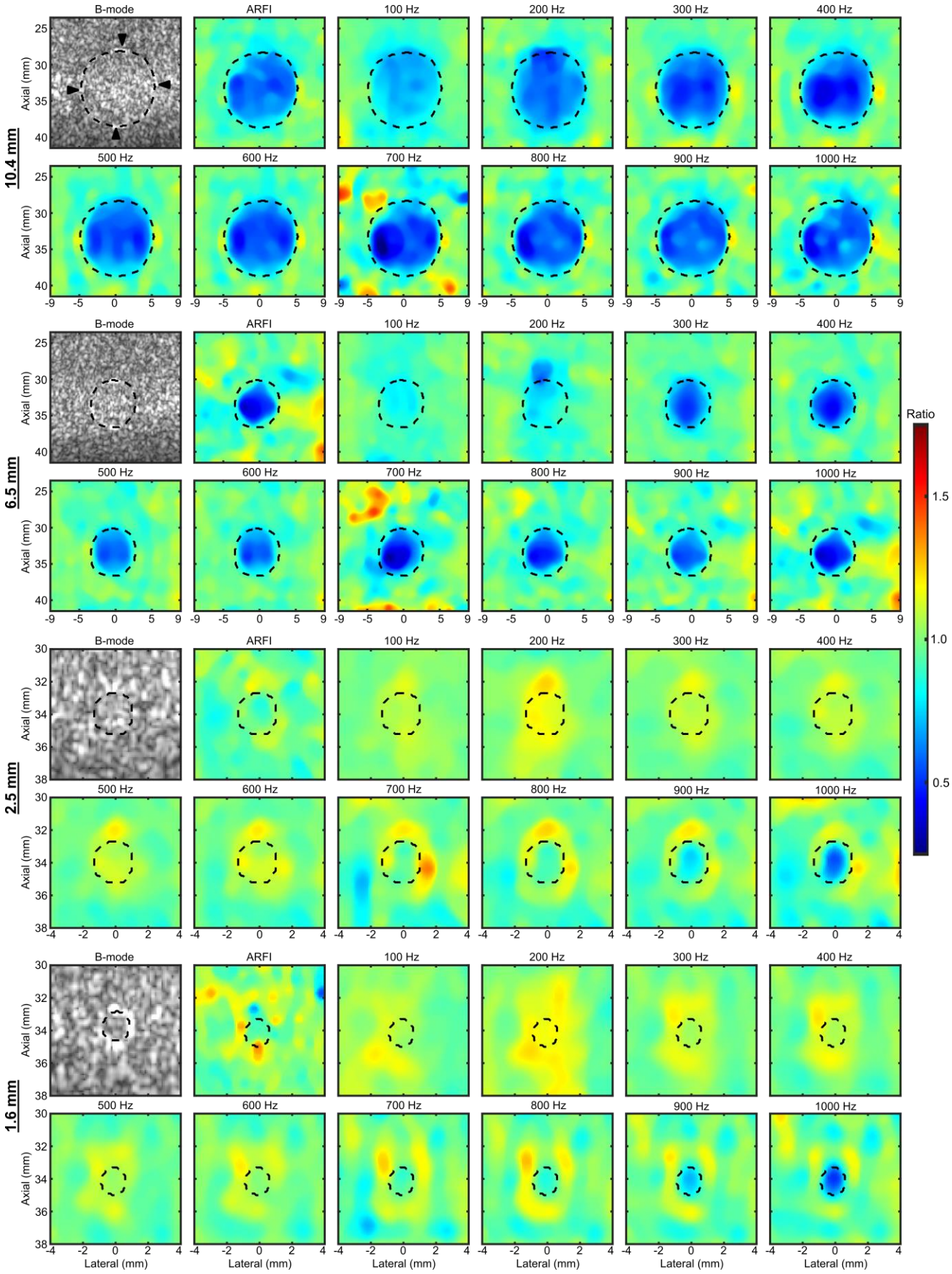

Fig 6: Bmode, ARFI normalized peak displacement, and ST-HMI normalized peak-to-peak displacement image at 100:100:1000 Hz of 36 kPa inclusion with 10.4 mm (1st-2nd rows), 6.5 mm (3rd-4th rows), 2.5 mm (5th – 6th rows), and 1.6 mm (7th – 8th rows) diameters.Black contour and arrowhead represent the inclusion boundary and the presence of high echogeneous region in the bournady, respectively.

Fig 5. The maximum CNR and contrast were achieved at 1000 and 900 Hz which were significantly higher than other

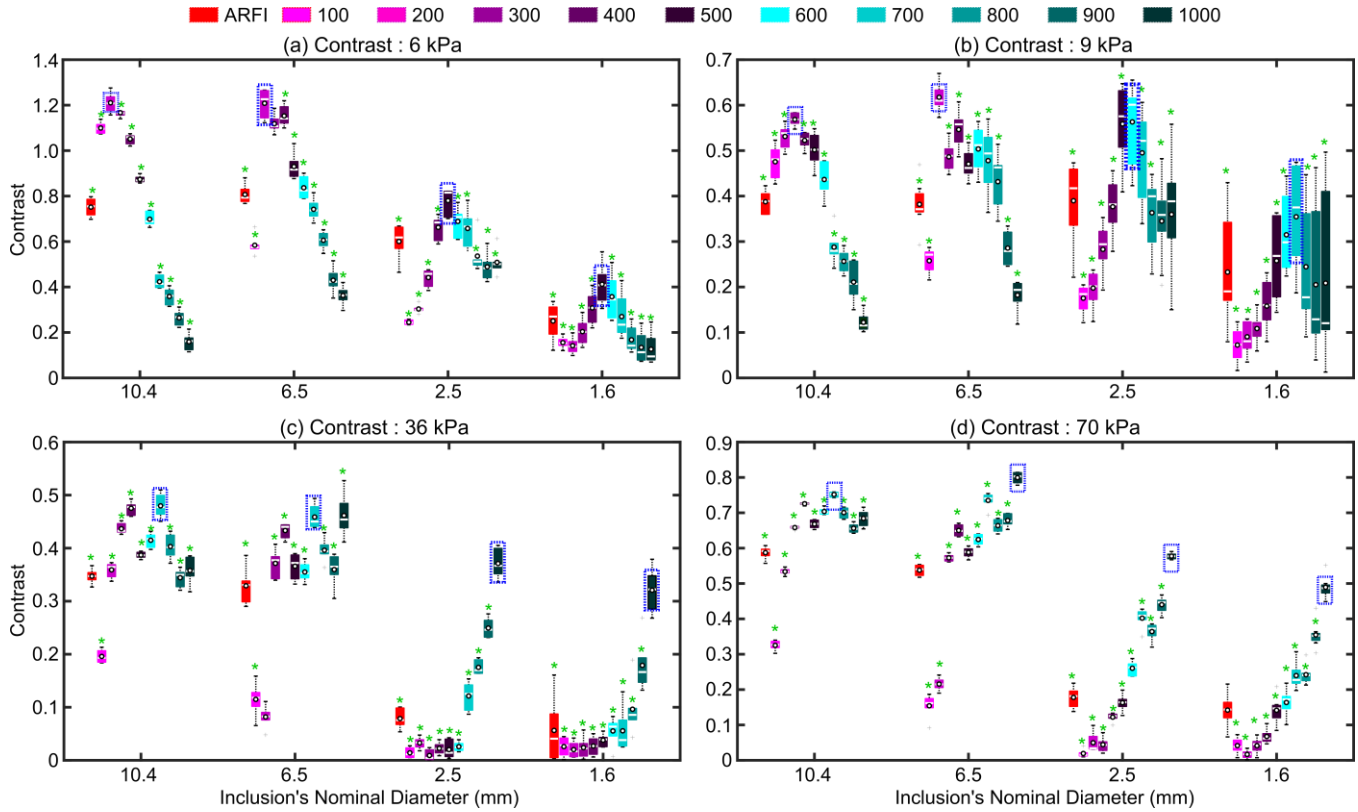

Fig 7: Contrast of ARFI (red box) and ST-HMI derived images at 100-1000 Hz of (a) 6, (b) 9, (c) 36, and (b) 70 kPa inclusions with 10.4, 6.5, 2.5, and 1.6 mm diameters embedded in an 18 kPa background. Note that, the Y-axis range is different between panels. ST-HMI derived images at 100-500 and 600-1000 Hz are shown in different combination of red+blue and green + blue colors. Data are plotted as median ± 0.5*interquartile range over 6 repeated acquisitions. The Kruskal–Wallis test suggested that contrast were statistically different across ARFI and ST-HMI at 100-1000 Hz irrespective of inclusion size and stiffness. For clarity, the asterisk is only shown when Kruskal–Wallis test suggests a statistical difference and median contrast were statistically different (sign ranksum) from the highest median contrast (dotted blue rectangle).

frequencies and PD ($p<0.05$, *kruskalwallis* and *ranksum*).

Fig. 6 shows representative ARFI PD and ST-HMI P2PD images at 100:100:1000 Hz of 36 kPa inclusion with 10.4, 6.5, 2.5, and 1.6 mm diameters. Note, all images were normalized to account for the variation in the ARF magnitude over axial distance. Four observations are notable. First, the perceived contrast of inclusion varies with the inclusion size for the fixed 36 kPa stiffness irrespective of ARFI or ST-HMI. Second, qualitatively ARFI detected 10.4 and 6.5 mm inclusions but was unable to detect 2.5 or 1.6 mm inclusion. Third, ST-HMI detected all inclusions, and the perceived contrast varied with the frequency. This result indicates that the frequency in ST-HMI can be exploited to detect different size inclusions with the same stiffness. Fourth, the number of frequencies detected inclusions decreases with size. As an example, all frequencies detected 10.4 mm inclusion whereas only 900 and 1000 Hz detected 1.6 mm inclusion.

Fig. 7 quantitatively compares ARFI versus ST-HMI derived contrast of 6 kPa (panel (a)), 9 kPa (panel (b)), 36 kPa (panel (c)), and 70 kPa (panel (d)) inclusions with 10.4, 6.5, 2.5, and 1.6 mm diameters. Five observations are notable. First, the contrast was statistically different ($p<0.05$, *kruskalwallis* test) between ARFI and ST-HMI at 100:100:1000 Hz irrespective of inclusion sizes or stiffnesses. Second, the frequency of ST-HMI can be exploited to achieve higher contrast ($p<0.05$, *ranksum* test) than ARFI. Third, the maximum contrast depends on the inclusion size and stiffness. Fourth, for fixed stiffness, maximum contrast decreases with inclusion size. Fifth, the frequency at which the maximum contrast was achieved also depended on the inclusion stiffness and size. The maximum contrast was achieved at (200, 200, 500, 500), (300, 200, 500, 700), (600, 700,1000, 1000), and (700, 1000,100,1000) Hz frequency for 6, 9, 36, and 70 kPa inclusions with (10.4, 6.5, 2.5,1.6) mm diameters, respectively.

Fig. 8 quantitatively compares ARFI versus ST-HMI derived CNR of 6 kPa (panel (a)), 9 kPa (panel (b)), 36 kPa (panel (c)), and 70 kPa (panel (d)) inclusions with 10.4, 6.5, 2.5, and 1.6 mm diameters. Observations similar to the contrast in Fig. 7 can be made i.e., the frequency of ST-HMI can be exploited to achieve higher CNR than ARFI and maximum CNR depends on frequency and inclusion's size and stiffness. However, the frequencies at which the maximum CNR was achieved were different from those at the maximum contrast. The maximum CNR was at achieved (300, 500, 900, 700), (300, 300, 600, 600), (300, 400, 1000, 1000), and (600, 900, 1000, 1000) Hz frequency for 6, 9, 36, and 70 kPa inclusions with (10.4, 6.5, 2.5,1.6) mm diameters, respectively. Note, only median values versus median and standard deviation were used in contrast versus CNR calculation, respectively. Therefore, CNR accounts for the heterogeneity of background and inclusion. CNR greater than 1 is needed to reliably detect inclusion.

Fig. 9 shows linear regression between ARFI PD ratio or ST-HMI P2PD ratio of background over inclusion versus Young's moduli ratio of inclusion over background with R^2, slope, and

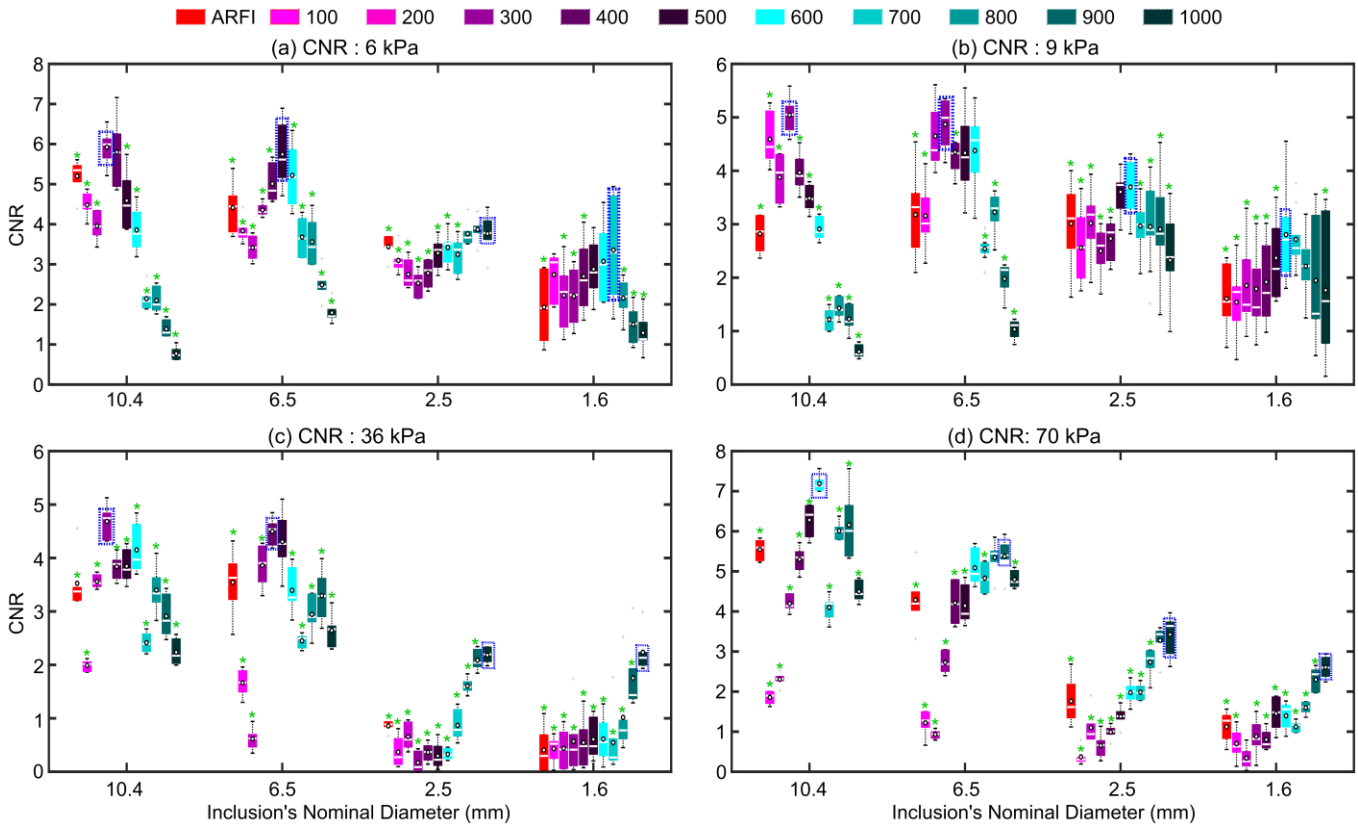

Fig 8: CNR of ARFI (red box) and ST-HMI derived images at 100-1000 Hz of (a) 6, (b) 9, (c) 36, and (b) 70 kPa inclusions with 10.4, 6.5, 2.5, and 1.6 mm diameters embedded in an 18 kPa background. Note that, the Y-axis range is different between panels. ST-HMI derived images at 100-500 and 600-1000 Hz are shown in different combination of red+blue and green + blue colors. Data are plotted as median ± 0.5*interquartile range over 6 repeated acquisitions. The Kruskal–Wallis test suggested that CNR were statistically different across ARFI and ST-HMI at 100-1000 Hz irrespective of inclusion size and stiffness. For clarity, the asterisk is only shown when Kruskal–Wallis test suggests a statistical difference and median contrast were statistically different (sign ranksum) from the highest median contrast (dotted blue rectangle).

root mean square error (RMSE) for 10.4 mm diameter. The results are only shown for 200-1000 Hz in steps of 200 Hz for simplicity. The RMSE was calculated between the displacement ratio and Young's moduli ratio. Table II lists R^2, slope, and RMSE of all frequencies for all 4 diameters and after combining all diameters. Combining all diameters means the size of the inclusion was not taken into consideration. For the larger inclusion (10.4 and 6.5 mm), 400 Hz had the lowest RMSE whereas 1000 Hz had the lowest RMSE for smaller inclusion (2.5 and 1.7 mm) along with combined diameter. Except for 100-300 Hz in combined diameters, the R^2 value was greater than 0.9 in all cases.

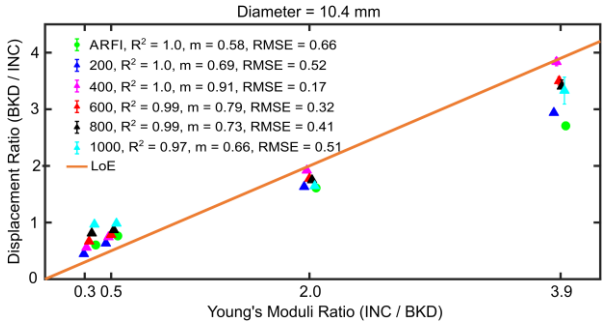

Fig 9: ST-HMI-derived Peak-to-peak displaceement (P2PD) and ARFI-derived peak displacment (PD) ratio of background (BKD) to inclusion (INC) versus Young's moduli ratio of inclusion to background for 10.4 mm diameter inclusion with R^2, slope (m), and root mean square error (RMSE) value on the legend. The numerator and denominator are interchanged in the abscissa and ordinate's ratio as Young's modulus and P2PD/PD are inversely related. Data are plotted as median ± 0.5* interquartile range over 6 repeated acquisitions. LoE = Line of Equivalency.

Fig. 10 shows *in vivo* B-mode, ARFI normalized PD, and ST-HMI normalized P2PD images at 100-1000 Hz of a mouse tumor on Day 6, 12, and 19. Table II lists CNR, contrast, and the displacement ratio (DR) of ARFI and ST-HMI images at three-time points. The DR was calculated as the ratio of ARFI PD or ST-HMI P2PD of neighboring non-cancerous tissue over the tumor. Therefore, higher DR means higher stiffness of tumor assuming that non-cancerous tissue stiffness remained stable over time. Six observations are notable. First, both ARFI and ST-HMI detected the presence of the tumor. Second, the tumor grew in size over time with the ingression of cancerous cells and the tumor area was 11.4, 19.2, and 56.0 mm^2 on Day 6, 12, and 19 respectively. Third, the tumor also became stiffer over time which was indicated by an increase in DR over time irrespective of methods or frequencies. Fourth, the CNR of ST-HMI-derived images was higher than ARFI irrespective size or stiffness of the tumor. Fifth, the CNR of ST-HMI-derived images increased with frequency for the tumor on Day 6 whereas the CNR remained stable with frequency for the tumor on Day 12 and 19. Sixth, the contrast of ARFI and ST-HMI images was similar.

IV. Discussion

Conventional HMI uses AM-ARF to interrogate mechanical properties by oscillating tissue at a particular frequency. To do so, HMI simultaneously generates and tracks narrowband

Table II

R^2, SLOPE, AND ROOT MEAN SQUARE ERROR (RMSE) OF LINEAR REGREESION BETWEEN ST-HMI / ARFI DISPLACEMENT RATIO (DR) VERSUS YOUNG'S MODULI (YM) RATIO IN PHANTOM FOR 10.4, 6.5, 2.5, 1.4 MM INCLUSION DIAMETERS AND AFTER COMBING ALL DIAMETER INCLUSIONS. $DR_{ST\text{-}HMI}$ = $P2PD_{BKD}$ / $P2PD_{INC}$ AND YM RATIO = YM_{INC} / YM_{BKD}, INC = INCLUSION, BKD= BACKGROUND. ST-HMI AND ARFI-DERIVED CNR, CONTRAST, AND DR OF MOUSE TUMOR. THE LOWEST RMSE AND HIGHEST CNR AND CONTRAST ARE SHOWN IN BOLD FOR BETTER DISTINCTION.

Diameter	Metric	ARFI	100	200	300	400	500	600	700	800	900	1000
10.4 mm	R^2	1.0	0.97	1.0	1.0	1.0	1.0	0.99	0.98	0.99	0.99	0.97
	Slope	0.58	0.42	0.69	0.76	0.91	0.73	0.79	0.93	0.73	0.61	0.66
	RMSE	0.66	1.01	0.52	0.36	**0.17**	0.41	0.32	0.30	0.41	0.57	0.51
6.5 mm	R^2	1.0	0.94	1.0	1.0	1.0	1.0	1.0	0.98	0.99	0.98	0.96
	Slope	0.54	0.25	0.46	0.75	0.84	0.61	0.68	1.02	0.74	0.71	1.14
	RMSE	0.74	1.28	0.97	0.41	**0.25**	0.62	0.49	0.31	0.38	0.44	0.61
2.5 mm	R^2	1.0	0.96	0.91	0.99	0.99	0.99	0.99	0.98	1.0	1.0	0.99
	Slope	0.22	0.08	0.10	0.21	0.26	0.27	0.32	0.43	0.34	0.38	0.55
	RMSE	1.36	1.53	1.57	1.38	1.32	1.30	1.22	1.03	1.13	1.02	**0.71**
1.6 mm	R^2	0.99	0.95	0.91	0.98	0.97	0.98	0.97	0.97	0.98	0.99	1.0
	Slope	0.24	0.10	0.12	0.22	0.27	0.27	0.30	0.35	0.32	0.39	0.56
	RMSE	1.33	1.51	1.54	1.40	1.33	1.34	1.30	1.18	1.18	1.02	**0.70**
Combined	R^2	0.94	0.87	0.81	0.89	0.94	0.98	0.99	1.0	0.99	1.0	0.99
	Slope	0.26	0.15	0.15	0.23	0.27	0.29	0.32	0.43	0.36	0.41	0.60
	RMSE	1.25	1.44	1.50	1.34	1.25	1.22	1.17	0.95	1.07	0.93	**0.60**
Mouse Day 6	CNR	5.48	8.3	6.68	7.62	7.07	7.86	7.73	7.71	8.47	**9.39**	9.35
	Contrast	0.82	0.72	0.78	0.80	**0.84**	0.81	0.81	0.80	0.79	0.78	0.74
	DR	5.53	3.60	4.45	5.02	6.13	5.14	5.18	5.02	4.69	4.52	3.81
Mouse Day 12	CNR	4.95	**6.97**	4.19	6.33	5.16	6.95	6.90	6.81	6.59	6.62	5.49
	Contrast	0.78	0.80	0.80	**0.84**	**0.84**	0.79	0.80	0.79	0.79	0.79	0.81
	DR	4.49	4.96	5.07	6.12	6.34	4.75	5.0	4.84	4.75	4.80	5.31
Mouse Day 19	CNR	1.79	3.84	3.25	3.83	3.63	4.28	**4.30**	4.18	4.07	3.93	3.86
	Contrast	**0.92**	0.88	**0.92**	0.91	**0.92**	0.88	0.88	0.88	0.87	0.86	0.85
	DR	11.9	8.50	12.3	11.6	11.8	8.31	8.35	8.40	7.56	7.28	6.81

harmonic oscillation with a frequency less than 100 Hz using focused ultrasound and imaging transducers, respectively [58]. To facilitate data acquisition, ST-HMI has been proposed recently and the feasibility of generating ST-HMI-induced oscillation in the range of 60-420 Hz was demonstrated by collecting each frequency data separately [43]. Though oscillation frequency can be exploited to better detect inclusions/lesions, acquisition of multiple frequencies separately may be unrealistic in clinical settings due to patients' or sonographer hand movements. To facilitate the generation of displacement maps at several frequencies simultaneously, this study presents a novel excitation pulse with frequencies from 100-1000 Hz for ST-HMI.

ST-HMI assesses mechanical properties "on-axis" to the ARF and is different from the "off-axis" shear wave-based methods like supersonic shear imaging [59], shear wave imaging (SWI) [60], shearwave dispersion ultrasound vibrometry [14], or harmonic SWI [8] in terms of estimating the mechanical properties of tissues. Though an excitation pulse composed of a sum of sinusoids was used in shear wave-based methods [16], there are several differences between the proposed work versus Zheng *et al.* [16]. First, Zheng *et al.* is a shear wave method. Therefore, the advantages of assessing mechanical properties "on-axis" to ARF as mentioned previously and also in [43] are still held. Second, Zheng *et al.* used two different transducers for generating multi-frequency excitation pulse and tracking induced motion "off-axis" to ARF whereas the proposed work uses a single transducer to perform both generation and tracking of motion. Third, Zheng *et al.* demonstrated the feasibility of generating multi-excitation motion in the homogeneous material only whereas this work has shown the feasibility in 16 different inclusions with varying stiffnesses and sizes and tumors in a mouse model, *in vivo*.

The proposed continuous excitation pulse was generated by summing sinusoids with the frequency of 100-1000 Hz and larger weights to the higher frequencies (j^2 in (1)). The frequency range was chosen by considering hardware constraints and previous research on shear wave-based methods [20], [61]. If the frequency lower than 100 Hz was chosen, the excitation pulse duration and data collection time will be longer albeit with better performance due to finer sampling. On the other hand, some frequency components may not have sufficient energy to generate displacements above the noise level if the frequencies higher than 1000 Hz are chosen while keeping the lower limit to 100 Hz. While the current frequency range of 100-1000 Hz was shown capable of generating displacement images over a wide range of stiffness (6-70 kPa) and size (1.6-10.4 mm), the performance of ST-HMI can be improved further by obtaining the data collection in two steps. In the first step, the data can be collected in a wider frequency range (200 – 2000 Hz) with a coarse sample of 200 Hz, then a narrow frequency range around the best performing frequency that can be used in the second step. This two-step data collection will lengthen the overall data collection duration. Therefore, there is a trade-off between improving lesion boundary delineation and data collection duration which will be dictated by the clinical applications.

The energy of the 100-1000 Hz frequency component of the continuous excitation pulse increased monotonically with frequency due to larger weights to the higher frequencies (Fig. 2b). However, the energy of frequency components of the discrete excitation pulse did not increase monotonically (Fig. 2b) due to sparse sampling (Fig. 2a). The energy was generally higher for larger frequencies except at 700 Hz. The displacement frequency spectrum (Fig. 3d) followed a similar relation of FT

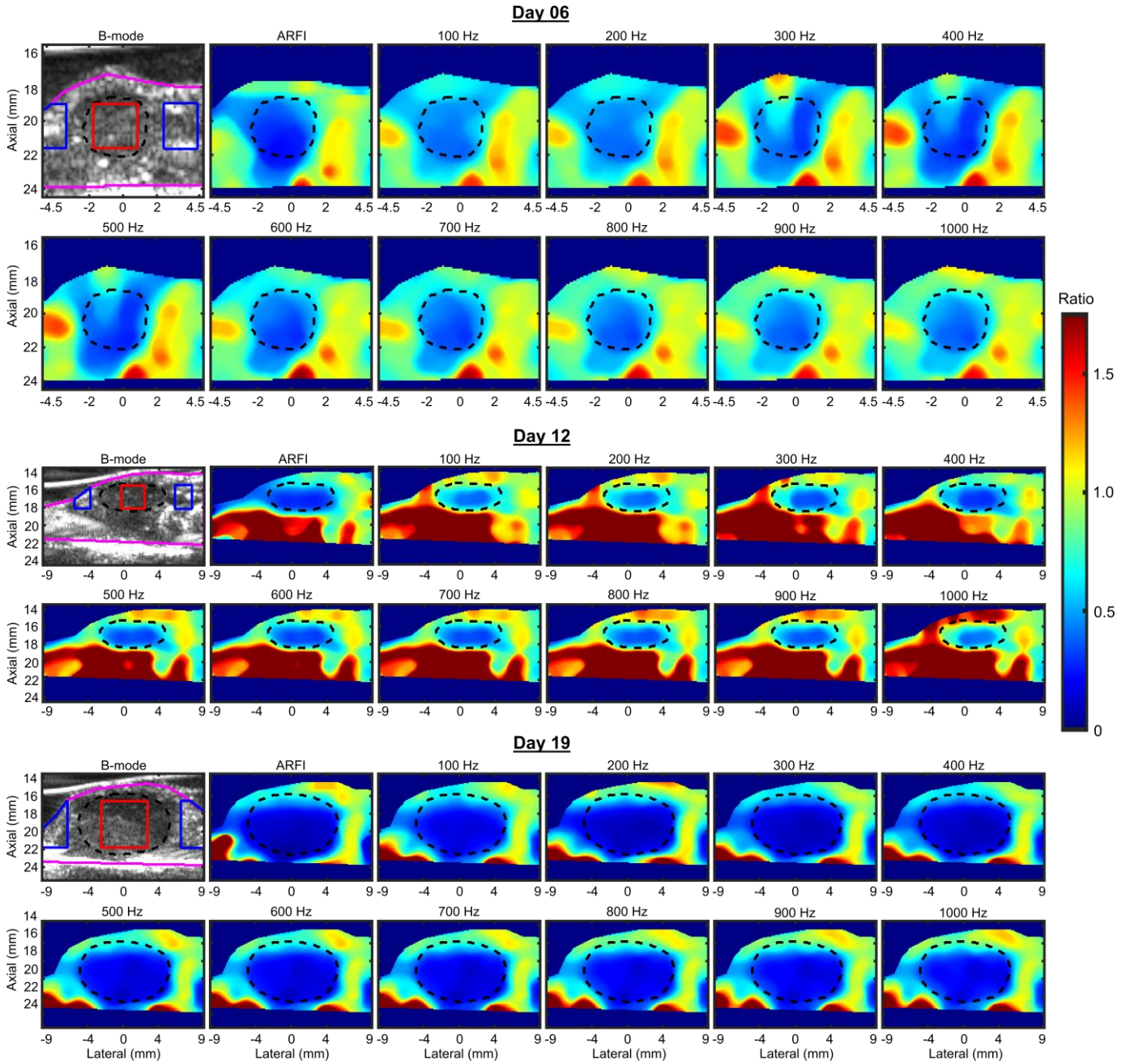

Fig 10: *In Vivo* Bmode, ARFI-derived normalized peak displacement, and ST-HMI derived normalized peak-to-peak displacement image at 100-1000 Hz of a 4T1 mouse tumor on Day 6 (1st-2nd rows), Day 12 mm (3rd-4th rows), and Day 19 (5th – 6th rows) post-injection of tumor cell. Black, magenta, red, and blue contours represent tumor boundary, displacement image field of view, the region of interest in tumor and neighboring non-cancerous tissue, respectively.

magnitude versus frequency as in the discrete excitation pulse. The result indicates that the FT magnitude spectrum of the discrete excitation pulse can be used to predict the FT magnitude spectrum of displacements. This is advantageous in customizing discrete excitation pulse based on the clinical application. Though the energy content of each frequency of discrete excitation pulse was different, the same excitation pulse was used to interrogate both background and inclusion. Therefore, normalized P2PD reflects the difference in mechanical properties between inclusion and background. Previous work also demonstrated that there was no significant difference in contrast or CNR of single frequency ST-HMI-derived images due to the difference in energy content of the oscillation frequency [43].

In this study, displacement was estimated using the 1-D NCC method [50]. While a deep convolutional neural networks-based motion estimator is proposed for ARFI imaging [62] with comparable performance to the Loupass phase-based displacement estimator, the NCC estimator generally provides higher accuracy than phase-based displacement estimators [50]. While the 2-D regularization-based displacement estimators [63]–[65] provide better axial displacement estimates in ultrasound quasi-static elastography, the displacement in the ARF-based methods is different from the quasi-static elastography in two ways. First, ARF generates stress predominantly in the axial direction which generally induces axial displacements of 0-20 μm and lateral displacements in the picometer range. Therefore, ARF-induced axial strain (<0.01%)

is very small compared to the larger strain (5-10%) in quasi-static elastography. Due to these smaller strains, signal decorrelation does not pose a problem in the ARF-induced displacement estimator. Second, 2-D ARFI or ST-HMI image was generated by exciting each lateral location (interval 0.3 or 0.6 mm) independently. Therefore, combining 2 or more lateral lines in displacement estimation means combining more decorrelated signals which will increase the variance in the displacement estimator.

The displacements at frequencies corresponding to the frequencies of the excitation pulse were calculated by adaptively finding the cutoff values of the bandpass filter (Fig. 3d). The passband of each frequency component will be different at the center of the inclusion versus near boundary or two different axial locations due to the variation in the ARF expiation beam point spread function (PSF) dimension. Note that, the ARF excitation PSF dimension varies with axial location with the smallest area at the focal depth. Due to the passband variation of each frequency component over spatial location, a custom algorithm was applied to find cutoff values at each pixel for bandpass filtering for each frequency component [43]. This adaptive bandpass filter cutoff is important to reduce the heterogeneity of the image. Adaptively finding the cut-off values is a faster process and usually takes 0.014 s for each pixel and frequency. One way to reduce the processing time is to calculate cut-off values at a 1 mm spatial interval instead of each pixel. Future work will explore the tradeoff between spatial intervals for calculating cut-off values versus image quality. The differential displacement profiles also contained higher harmonic frequencies (i.e., greater than 1000 Hz). Displacement at higher harmonic frequencies was not exploited because the energy of the frequency greater than the frequency of the excitation pulse is less controllable and depends on the relative location of the pixel.

The feasibility of generating 2-D images at 100-1000 Hz using the proposed multi-frequency excitation pulse was tested *in silico*, in phantom, and in a breast cancer mouse tumor *in vivo* with comparison to ARFI imaging in terms of CNR and contrast. While both ARFI and ST-HMI detected the presence of a low elastic contrast spherical inclusion in an *in silico* phantom (Fig. 4), maximum contrast and CNR were achieved by ST-HMI at 900 and 1000 Hz, respectively (Fig. 5). The advantage of generating P2PD at different frequencies simultaneously to delineate different sized 36 kPa inclusions in a commercial phantom is qualitatively demonstrated in Fig. 6. Qualitatively, ARFI and P2PD images (frequency ≥ 300 Hz) detected 10.4 and 6.5 mm inclusions. However, 2.5 and 1.6 mm inclusions were not detected by ARFI whereas P2PD images at 900 and 1000 Hz were able to detect 2.5 and 1.6 mm inclusions. The background of 10.4 and 6.5 mm inclusion was noisier, especially at 700 Hz than other inclusion. It may be due to the presence of heterogeneity in the background which is picked up by 700 Hz or the corruption of 700 Hz by some kind of noise due to the lowest energy in 700 Hz. More investigations are needed to find the source of this particular noise.

The further advantage of exploiting frequency to delineate inclusions with different sizes and stiffnesses is demonstrated quantitatively in Figs. 7 and 8. The maximum CNR and contrast achieved by ST-HMI were higher than ARFI irrespective of size and stiffness of inclusions. In addition, the highest CNR and contrast were achieved at different frequencies depending on the inclusion size and stiffness. As the size and stiffness of the lesions or tumors are not known apriori, it is impossible to achieve maximum CNR and contrast using a single frequency. The main advantage of the proposed multi-frequency excitation pulse is that there is no need for apriori knowledge of lesions or tumors size or stiffness to achieve maximum CNR and contrast. These results demonstrate an advantage of using a multi-frequency excitation pulse to simultaneously generate displacement maps at different frequencies instead of using a pulsed excitation pulse to generate displacement profiles with a wide frequency range as it is done in ARFI or single frequency ST-HMI.

The general trend in ST-HMI-derived CNR and contrast is that the frequency, at which maximum CNR and contrast were achieved, increases with stiffnesses for fixed-size inclusion and decreases with size for fixed stiffness inclusion. This is expected. Because, in a material with fixed stiffness, the wavelength of the generated shear waves within the ARF excitation beam will be smaller for higher frequency. Therefore, higher frequencies are better to contrast smaller inclusions. Similarly, the wavelength will be larger for the stiffer materials (i.e., higher shear wave speed) for a fixed frequency [43]. However, the inclusion can be detectable even if a sub-wavelength of a particular frequency is contained within the inclusion, and the contrast of inclusion increases with the increasing ratio of diameter over wavelength. As an example, the wavelength of 400, 500, and 1000 Hz in a 22.5 kPa *in silico* inclusion is 6.85, 5.48, and 2.74 mm, respectively. Note that, the inclusion was not detectable at 400 Hz but the detectability or contrast of the inclusion increases with frequency from 500 to 1000 Hz (Figs. 4 and 5). The ratio of inclusion diameter (2 mm) over wavelength is 0.3, 0.36, and 0.73 at 400, 500, and 1000 Hz, respectively. Therefore, the detection of the inclusion is feasible even if 36% of a wavelength is contained within the inclusion. Note, the detectability of the inclusion also depends on the ARF excitation beam PSF dimension in the lateral and elevation plane. The lateral and elevational dimension of the ARF excitation beam was fixed to 0.8 and 1.4 mm for *in silico* model and all phantom experiments. Future studies will investigate the spatial resolution of ST-HMI by considering both the oscillation frequency and PSF dimension. Note, the ST-HMI interrogates mechanical properties at the ARF-ROE without observing shear wave propagation away from the ARF-ROE. Therefore, the frequency is exploited to better detect inclusion due to the shearing within the ARF excitation beam. Shearing is occurred due to the nonuniform axial displacements within the ARF excitation beam PSF [48], [66].

The CNR and contrast mainly increased with frequency until they reached maximum, and then decreased with frequency for 6 and 9 kPa inclusion irrespective of size. However, the CNR and contrast increased with frequency for 36 and 70 kPa inclusions with 2.5 and 1.6 mm diameters which suggests that further optimization in ST-HMI performance is possible by using a higher frequency for these inclusions. Future works will test the feasibility of using frequencies up to 2000 Hz.

The contrast is not reciprocal between 9 kPa versus 36 kPa inclusions. This phenomenon is more pronounced for the smaller inclusions which may be due to bulk displacement of the inclusion as the focal zone of the ARF excitation beam was around 10 mm. The discord in the contrast between ARFI-derived images of 9 versus 36 kPa is higher than in ST-HMI images (Fig. 7). The ARFI contrast was approximately 5 times higher in 9 versus 36 kPa with 2.5 and 1.6 mm diameter whereas the maximum median ST-HMI contrast was 1.2-1.6 times higher in 9 versus 36 kPa with the maximum difference for 2.5 mm diameter inclusion. It is reasonable to expect that the maximum contrast of 36 kPa with 2.5 and 1.6 mm diameter inclusions will increase if the ST-HMI data were collected at a frequency beyond 1000 Hz. This is another advantage of using a multi-frequency excitation pulse so that the contrast difference can be reduced between softer versus stiffer or different sized inclusions with the same true elastic contrast difference.

The diminished contrast at 100 or 200 Hz may not be due to the minimal energy at those frequencies. As an example, while the contrast of a 6.5 mm 36 kPa inclusion was maximum at 700 Hz (Fig. 7), the peak-to-peak displacement (P2PD) was 0.17 and 0.05 μm at the center of the inclusion for 100 and 700 Hz respectively. Despite the lower displacement, the highest contrast was achieved at 700 Hz. Note, the displacement estimated by NCC was in the range of 1-5 μm (Fig. 3b). However, P2PD became sub-micron after differential displacement calculation and filtering out each frequency component. In addition, 200 Hz provided the maximum contrast for the 10.4 and 6.5 mm, 6 kPa inclusions. If it is due to minimal energy, maximum contrast should not be achieved at 200 Hz. Therefore, the frequency at which maximum contrast and CNR were achieved depends mainly on the size and stiffness of the inclusion.

While delineating the true boundary of lesions is useful in surgical planning or guiding biopsy or monitoring the response of the treatment, like, shrinkage of tumors due to the chemotherapy response, the P2PD ratio of background over inclusion has the potential to be used as a relative stiffness indicator for longitudinal or cross-sectional studies [52]. Fig. 9 and Table II show that the P2PD ratio is highly correlated with Young's moduli irrespective of frequencies or inclusion sizes. However, the lowest RMSE was achieved at 400 and 1000 Hz for larger (10.4 and 6.5 mm) and smaller (2.5 and 1.6 mm) diameters, respectively which indicates that the size of the inclusion will confound the P2PD ratio derived relative stiffness assessment. Therefore, there is a need to develop a normalizing term accounting for the inclusion size before using the P2PD ratio as a relative stiffness indicator. Note, a similar confounding effect of inclusion size on the ARFI PD ratio was also observed. However, the P2PD ratio at 1000 Hz had lower RMSE than ARFI irrespective of size or after combining all diameters. The future study will investigate the use of either the P2PD ratio at 1000 Hz or the P2PD ratio at each frequency with a normalizing term to monitor disease progression or regression.

These results in the phantoms are very promising. However, phantoms are the idealistic representation of tissues. *In vivo* performance of ST-HMI was evaluated by imaging a 4T1 mouse tumor on Day 6, 12, and 19. While ARFI and ST-HMI-derived DR indicated the tumor became stiffer over time, the size of the tumor was not taken into account. As discussed previously related to Fig. 9 and Table II, the size of the tumor will confound the DR change over time. While ARFI normalized PD was lower than ST-HMI normalized P2PD in the tumor, especially on Day 6, ST-HMI at 400 Hz achieved the highest contrast (Table II) because normalized P2PD was higher than PD in the nearest non-cancerous tissue. Similar to phantoms, the CNR of ST-HMI images was higher than ARFI and increased with frequency, especially for the smaller tumor on Day 6. Note, the change in CNR with frequency was higher in the phantom (Fig. 8) than in the tumor. It may be due to the change in ROI in the tumor (rectangle, Fig. 10) from the phantom (circle, Fig. 3) for CNR calculation. As there is no background/non-cancerous tissue concentric to the tumor, rectangle ROI was used. As the displacement is calculated "on-axis" to ARF, the boundary is distorted more in the axial than lateral direction (Figs. 4 and 6). While the perceived detectability of the tumor was higher for larger the tumor, the CNR of the larger tumor was the lowest irrespective of methods. It may be due to either not having enough non-cancerous tissue ROI for the CNR calculation or the tumor along with neighboring tissues becomes heterogeneous over time. Future studies with histopathological validation will be performed to answer this question.

In this study, B-mode-derived boundary was used as comparative benchmarks rather than ground truth boundary to select ROI for the CNR and contrast calculation. While there was no noticeable difference in echogenicity between inclusion and background, there is a slight change in the echogenicity at the boundary (arrowhead in Fig. 6) which guides us to draw the boundary. In addition, the inclusion's ROI area was smaller than the inclusion size. Therefore, the effect of boundary derivation will be minimal for comparing ARFI and ST-HMI images as the same ROI, correctly located in background and inclusion, was used for CNR and contrast calculation. As this study demonstrates that multi-frequency ST-HMI can detect inclusions at different sizes and stiffnesses, future studies aim to develop techniques for automated boundary detection based on the multi-frequency displacement images.

While multi-frequency ST-HMI demonstrated better contrast and CNR than ARFI, the data collection and processing time is higher in ST-HMI compared to the ARFI (Table I). Due to the separation (at least 1 ms) of the discrete excitation pulses (Fig. 2a), the temperature rise due to ST-HMI was less than 1ºC which is within the U.S. FDA limits [43], [67]. ARFI-derived PD image is used as a comparative benchmark of the "on-axis" displacement image because PD has already been used to characterize different biological tissues [51], [68]–[71]. However, CNR, contrast, and resolution of ARFI-derived displacement images can be improved by generating displacement images at different time points [30] which also makes it very difficult to compare with ST-HMI. As the contrast is usually maximized at later time points, especially for softer inclusions, observed displacements are a combination of the recovery and the reflected shear wave, which makes their magnitude become unreliable and results in decreased resolution [30]. In addition, later time points are more susceptible to being corrupted by motion artifacts and may show a reversal of

inclusion contrast i.e. stiffer inclusion may appear as a softer or vice versa [57]. Future studies will be conducted to perform a detailed comparison of ARFI-derived optimized displacement, multi-frequency ST-HMI-derived P2PD, and shear wave-derived group and phase velocity images in terms of CNR, contrast, and resolution with or without the presence of motion artifacts.

This feasibility study of generating multi-frequency oscillation simultaneously using the proposed excitation pulse demonstrated very promising results. However, the study has four main limitations. First, only two examples of the combination of excitation and tracking pulses were demonstrated. In theory, a different combination of discrete excitation pulse numbers and the location of discrete pulses can be used to generate 100-1000 Hz frequencies with varying amplitude. We hypothesize that results will not vary significantly depending on the excitation pulse number and location of the discrete pulse because the previous study showed that results were similar for the same frequency with different energy contents [43]. However, more experiments are needed to validate the hypothesis. Second, P2PD was used as a relative indicator of viscoelastic properties. In the future, filtered displacement profiles at each frequency can be fit to a well-known rheological model to separate the contributions of elasticity and viscosity [34], [35]. Future studies will also test the feasibility of correcting attenuation between cancerous versus healthy tissue using displacement at multiple frequencies. Third, the mechanical anisotropy of tumors [72] was ignored. In the future, the mechanical anisotropy will be assessed using P2PD at each frequency generated using two orthogonal point spread functions [49], [51], [73]. Fourth, there was no demonstration of the proposed multi-frequency pulse in humans. The translation of the proposed pulse in the clinics should be straightforward as the previous work using single-frequency ST-HMI has shown strong promise in delineating breast masses in humans [43]. One potential challenge is to provide enough energy at each frequency to exceed the noise floor, especially for deeper and stiffer tissue. One potential solution is to collect the data in two steps as mentioned earlier. Future works will apply the proposed multi-frequency pulse for imaging tumor masses in breast cancer patients.

V. Conclusion

In this study, the feasibility of generating ST-HMI-derived P2PD at multi-frequency was presented using an excitation pulse composed of a sum of sinusoids with frequency from 100 to 1000 Hz. The performance of the proposed excitation pulse was evaluated by imaging 16 different inclusions with varying stiffnesses and sizes and was compared to the ARFI imaging. The highest CNR and contrast were achieved at a frequency dependent on the inclusion size and stiffness. The maximum CNR and contrast achieved by ST-HMI were higher than ARFI irrespective of inclusion size and stiffness. The P2PD ratio is highly correlated with Young's moduli irrespective of frequencies or sizes with the lowest RMSE overserved at 1000 Hz. The P2PD ratio of non-cancerous tissue over tumors increased over time indicating stiffening of the tumor. ST-HMI was capable of detecting as small as 1.6 mm diameter inclusion in phantom. These findings indicate the advantages of using a multi-frequency excitation pulse to simultaneously generate oscillation at several frequencies to better delineate inclusions or lesions.

Acknowledgments

The authors thank Drs. Saurabh Singh, Indranil Basu, and Chandan Guha from the Albert Einstein College of Medicine & Montefiore Medical Center, Bronx, NY USA for providing the cancer cell for the mouse study and Niloufar Saharkhiz and Xiaoyue Li for the help in the mouse experiments.

References

[1] R. M. S. Sigrist, J. Liau, A. El Kaffas, M. C. Chammas, and J. K. Willmann, "Ultrasound Elastography: Review of Techniques and Clinical Applications," *Theranostics*, vol. 7, no. 5, pp. 1303–1329, 2017, doi: 10.7150/thno.18650.

[2] S. K. Venkatesh *et al.*, "Magnetic resonance elastography: beyond liver fibrosis—a case-based pictorial review," *Abdom. Radiol.*, vol. 43, no. 7, pp. 1590–1611, Jul. 2018, doi: 10.1007/s00261-017-1383-1.

[3] S. Wang and K. V. Larin, "Optical coherence elastography for tissue characterization: a review," *J. Biophotonics*, vol. 8, no. 4, pp. 279–302, Apr. 2015, doi: 10.1002/jbio.201400108.

[4] A. Arani, A. Manduca, R. L. Ehman, and J. Huston Iii, "Harnessing brain waves: a review of brain magnetic resonance elastography for clinicians and scientists entering the field.," *Br. J. Radiol.*, vol. 94, no. 1119, p. 20200265, Mar. 2021, doi: 10.1259/bjr.20200265.

[5] G. Rus, I. H. Faris, J. Torres, A. Callejas, and J. Melchor, "Why Are Viscosity and Nonlinearity Bound to Make an Impact in Clinical Elastographic Diagnosis?," *Sensors*, vol. 20, no. 8, p. 2379, Apr. 2020, doi: 10.3390/s20082379.

[6] H. Zhao *et al.*, "Noninvasive assessment of liver fibrosis using ultrasound-based shear wave measurement and comparison to magnetic resonance elastography.," *J. Ultrasound Med.*, vol. 33, no. 9, pp. 1597–1604, Sep. 2014, doi: 10.7863/ultra.33.9.1597.

[7] J. H. Yoon *et al.*, "Hepatic fibrosis: prospective comparison of MR elastography and US shear-wave elastography for evaluation.," *Radiology*, vol. 273, no. 3, pp. 772–82, Dec. 2014, doi: 10.1148/radiol.14132000.

[8] S. Sadeghi, C.-Y. Lin, and D. H. Cortes, "Narrowband Shear Wave Generation Using Sinusoidally Modulated Acoustic Radiation Force," *IEEE Trans. Ultrason. Ferroelectr. Freq. Control*, vol. 66, no. 2, pp. 264–272, Feb. 2019, doi: 10.1109/TUFFC.2018.2884847.

[9] J. R. Doherty, G. E. Trahey, K. R. Nightingale, and M. L. Palmeri, "Acoustic radiation force elasticity imaging in diagnostic ultrasound.," *IEEE Trans. Ultrason. Ferroelectr. Freq. Control*, vol. 60, no. 4, pp. 685–701, Apr. 2013, doi: 10.1109/TUFFC.2013.2617.

[10] L. Sandrin *et al.*, "Transient elastography: a new noninvasive method for assessment of hepatic fibrosis.," *Ultrasound Med. Biol.*, vol. 29, no. 12, pp. 1705–1713, 2003, doi: 10.1016/j.ultrasmedbio.2003.07.001.

[11] D. H. Cortes, S. M. Suydam, K. G. Silbernagel, T. S. Buchanan, and D. M. Elliott, "Continuous Shear Wave Elastography: A New Method to Measure Viscoelastic Properties of Tendons in Vivo.," *Ultrasound Med. Biol.*, vol. 41, no. 6, pp. 1518–29, Jun. 2015, doi: 10.1016/j.ultrasmedbio.2015.02.001.

[12] H. Zhao *et al.*, "External vibration multi-directional ultrasound shearwave elastography (EVMUSE): application in liver fibrosis staging.," *IEEE Trans. Med. Imaging*, vol. 33, no. 11, pp. 2140–8, Nov. 2014, doi: 10.1109/TMI.2014.2332542.

[13] J. Vappou, C. Maleke, and E. E. Konofagou, "Quantitative viscoelastic parameters measured by harmonic motion imaging," *Phys. Med. Biol.*, vol. 54, no. 11, pp. 3579–3594, Jun. 2009, doi: 10.1088/0031-9155/54/11/020.

[14] S. Chen *et al.*, "Shearwave dispersion ultrasound vibrometry (SDUV) for measuring tissue elasticity and viscosity.," *IEEE Trans. Ultrason. Ferroelectr. Freq. Control*, vol. 56, no. 1, pp. 55–62, Jan. 2009, doi: 10.1109/TUFFC.2009.1005.

[15] S. Sadeghi and D. H. Cortes, "Measurement of the shear modulus in thin-layered tissues using numerical simulations and shear wave elastography," *J. Mech. Behav. Biomed. Mater.*, vol. 102, no. September 2019, p. 103502, Feb. 2020, doi: 10.1016/j.jmbbm.2019.103502.

[16] Yi Zheng *et al.*, "Ultrasound vibrometry using orthogonal- frequency-based vibration pulses," *IEEE Trans. Ultrason. Ferroelectr. Freq. Control*, vol. 60, no. 11, pp. 2359–2370, Nov. 2013, doi: 10.1109/TUFFC.2013.6644739.

[17] S. Catheline *et al.*, "Measurement of viscoelastic properties of homogeneous soft solid using transient elastography: An inverse problem approach," *J. Acoust. Soc. Am.*, vol. 116, no. 6, pp. 3734–3741, Dec. 2004, doi: 10.1121/1.1815075.

[18] S. Chen *et al.*, "Assessment of liver viscoelasticity by using shear waves induced by ultrasound radiation force.," *Radiology*, vol. 266, no. 3, pp. 964–70, Mar. 2013, doi: 10.1148/radiol.12120837.

[19] M. Bhatt *et al.*, "Reconstruction of Viscosity Maps in Ultrasound Shear Wave Elastography.," *IEEE Trans. Ultrason. Ferroelectr. Freq. Control*, vol. 66, no. 6, pp. 1065–1078, Apr. 2019, doi: 10.1109/TUFFC.2019.2908550.

[20] P. Kijanka and M. W. Urban, "Local Phase Velocity Based Imaging: A New Technique Used for Ultrasound Shear Wave Elastography.," *IEEE Trans. Med. Imaging*, vol. 38, no. 4, pp. 894–908, Apr. 2019, doi: 10.1109/TMI.2018.2874545.

[21] E. Budelli *et al.*, "A diffraction correction for storage and loss moduli imaging using radiation force based elastography.," *Phys. Med. Biol.*, vol. 62, no. 1, pp. 91–106, 2017, doi: 10.1088/1361-6560/62/1/91.

[22] K. Nightingale *et al.*, "Derivation and analysis of viscoelastic properties in human liver: Impact of frequency on fibrosis and steatosis staging," *IEEE Trans. Ultrason. Ferroelectr. Freq. Control*, vol. 62, no. 1, pp. 165–175, 2015, doi: 10.1109/TUFFC.2014.006653.

[23] S. L. Lipman, N. C. Rouze, M. L. Palmeri, and K. R. Nightingale, "Impact of Acoustic Radiation Force Excitation Geometry on Shear Wave Dispersion and Attenuation Estimates," *Ultrasound Med. Biol.*, no. 2016, Feb. 2018, doi: 10.1016/j.ultrasmedbio.2017.12.019.

[24] M. W. Urban, B. Qiang, P. Song, I. Z. Nenadic, S. Chen, and J. F. Greenleaf, "Investigation of the effects of myocardial anisotropy for shear wave elastography using impulsive force and harmonic vibration," *Phys. Med. Biol.*, vol. 61, no. 1, pp. 365–382, Jan. 2016, doi: 10.1088/0031-9155/61/1/365.

[25] P. Kijanka and M. W. Urban, "Local Phase Velocity Based Imaging (LPVI) of Viscoelastic Phantoms and Tissues," *IEEE Trans. Ultrason. Ferroelectr. Freq. Control*, vol. 3010, no. c, pp. 1–1, 2020, doi: 10.1109/TUFFC.2020.2968147.

[26] K. Nightingale, M. S. Soo, R. Nightingale, and G. Trahey, "Acoustic radiation force impulse imaging: in vivo demonstration of clinical feasibility.," *Ultrasound Med. Biol.*, vol. 28, no. 2, pp. 227–35, Feb. 2002, Accessed: Dec. 07, 2014. [Online]. Available: http://www.ncbi.nlm.nih.gov/pubmed/11937286.

[27] M. M. Hossain *et al.*, "Viscoelastic Response Ultrasound Detects Changes in Degree of Mechanical Anisotropy with Renal Fibrosis in Pig Model," in *2019 IEEE International Ultrasonics Symposium (IUS)*, Oct. 2019, vol. 2019-Octob, pp. 415–418, doi: 10.1109/ULTSYM.2019.8925733.

[28] E. E. Konofagou and K. Hynynen, "Localized harmonic motion imaging: Theory, simulations and experiments," *Ultrasound Med. Biol.*, vol. 29, no. 10, pp. 1405–1413, 2003, doi: 10.1016/S0301-5629(03)00953-0.

[29] M. R. Selzo, C. J. Moore, M. M. Hossain, M. L. Palmeri, and C. M. Gallippi, "On the Quantitative Potential of Viscoelastic Response (VisR) Ultrasound Using the One-Dimensional Mass-Spring-Damper Model.," *IEEE Trans. Ultrason. Ferroelectr. Freq. Control*, vol. 63, no. 9, pp. 1276–87, 2016, doi: 10.1109/TUFFC.2016.2539323.

[30] P. J. Hollender, S. J. Rosenzweig, K. R. Nightingale, and G. E. Trahey, "Single- and Multiple-Track-Location Shear Wave and Acoustic Radiation Force Impulse Imaging: Matched Comparison of Contrast, Contrast-to-Noise Ratio and Resolution," *Ultrasound Med. Biol.*, vol. 41, no. 4, pp. 1043–1057, 2015, doi: 10.1016/j.ultrasmedbio.2014.11.006.

[31] S. S. Leong *et al.*, "Stiffness and Anisotropy Effect on Shear Wave Elastography: A Phantom and in Vivo Renal Study," *Ultrasound Med. Biol.*, vol. 00, no. 00, pp. 1–12, Oct. 2019, doi: 10.1016/j.ultrasmedbio.2019.08.011.

[32] Y. S. Cho, S. Lim, Y. Kim, T. Y. Kim, W. K. Jeong, and J. H. Sohn, "Abdominal Wall Thickness Affects Liver Stiffness Measurements by 2-D Shear Wave Elastography in Patients with Chronic Liver Disease," *Ultrasound Med. Biol.*, vol. 00, no. 00, pp. 1–7, Jul. 2019, doi: 10.1016/j.ultrasmedbio.2019.06.415.

[33] X. Zhao and A. a. Pelegri, "Dynamic Simulation of Viscoelastic Soft Tissue in Acoustic Radiation Force Creep Imaging," *J. Biomech. Eng.*, vol. 136, no. 9, p. 094502, 2014, doi: 10.1115/1.4027934.

[34] M. M. Hossain and C. M. Gallippi, "Viscoelastic Response Ultrasound Derived Relative Elasticity and Relative Viscosity Reflect True Elasticity and Viscosity: In Silico and Experimental Demonstration.," *IEEE Trans. Ultrason. Ferroelectr. Freq. Control*, vol. 67, no. 6, pp. 1102–1117, 2020, doi: 10.1109/TUFFC.2019.2962789.

[35] F. Viola and W. F. Walker, "Radiation force imaging of viscoelastic properties with reduced artifacts.," *IEEE Trans. Ultrason. Ferroelectr. Freq. Control*, vol. 50, no. 6, pp. 736–42, Jun. 2003, Accessed: Aug. 28, 2016. [Online]. Available: http://www.ncbi.nlm.nih.gov/pubmed/10870702.

[36] M. Fatemi and J. F. Greenleaf, "Vibro-acoustography: An imaging modality based on ultrasound-stimulated acoustic emission," *Proc. Natl. Acad. Sci.*, vol. 96, no. 12, pp. 6603–6608, 1999, doi: 10.1073/pnas.96.12.6603.

[37] M. W. Urban, M. Fatemi, and J. F. Greenleaf, "Modulation of ultrasound to produce multifrequency radiation force.," *J. Acoust. Soc. Am.*, vol. 127, no. 3, pp. 1228–38, Mar. 2010, doi: 10.1121/1.3294487.

[38] T. Payen *et al.*, "Elasticity mapping of murine abdominal organs in vivo using harmonic motion imaging (HMI)," *Phys. Med. Biol.*, vol. 61, no. 15, pp. 5741–5754, Aug. 2016, doi: 10.1088/0031-9155/61/15/5741.

[39] T. Payen *et al.*, "Harmonic Motion Imaging of Pancreatic Tumor Stiffness Indicates Disease State and Treatment Response," *Clin. Cancer Res.*, vol. 26, no. 6, pp. 1297–1308, Mar. 2020, doi: 10.1158/1078-0432.CCR-18-3669.

[40] C. Wu *et al.*, "Assessing Age-Related Changes in the Biomechanical Properties of Rabbit Lens Using a Coaligned Ultrasound and Optical Coherence Elastography System," *Invest. Ophthalmol. Vis. Sci.*, vol. 56, no. 2, pp. 1292–1300, Feb. 2015, doi: 10.1167/iovs.14-15654.

[41] Y. Han, S. Wang, T. Payen, and E. Konofagou, "Fast lesion mapping during HIFU treatment using harmonic motion imaging guided focused ultrasound (HMIgFUS) in vitro and in vivo," *Phys. Med. Biol.*, vol. 62, no. 8, pp. 3111–3123, Apr. 2017, doi: 10.1088/1361-6560/aa6024.

[42] J. Grondin, T. Payen, S. Wang, and E. E. Konofagou, "Real-time Monitoring of High Intensity Focused Ultrasound (HIFU) Ablation of In Vitro Canine Livers Using Harmonic Motion Imaging for Focused Ultrasound (HMIFU).," *J. Vis. Exp.*, vol. 2015, no. 105, p. e53050, Nov. 2015, doi: 10.3791/53050.

[43] M. M. Hossain, N. Saharkhiz, and E. E. Konofagou, "Feasibility of Harmonic Motion Imaging Using a Single Transducer: In Vivo Imaging of Breast Cancer in a Mouse Model and Human Subjects," *IEEE Trans. Med. Imaging*, vol. 40, no. 5, pp. 1390–1404, May 2021, doi: 10.1109/TMI.2021.3055779.

[44] M. M. Hossain, N. Saharkhiz, and E. E. Konofagou, "In Vivo Demonstration of Single Transducer Harmonic Motion Imaging (ST-HMI) in a Breast Cancer Mouse Model and Breast Cancer Patients," in *2020 IEEE International Ultrasonics Symposium (IUS)*, Sep. 2020, vol. 2020-Septe, pp. 1–4, doi: 10.1109/IUS46767.2020.9251522.

[45] J. A. Jensen, D.- Lyngby, P. Medical, B. Engineering, and I. Technology, "Field: A Program for Simulating Ultrasound Systems," in *10th Nordic-Baltic Conference on Biomedical Imaging*, 1996, vol. 34, pp. 351–353.

[46] J. A. Jensen and N. B. Svendsen, "Calculation of pressure fields from arbitrarily shaped, apodized, and excited ultrasound transducers.," *IEEE Trans. Ultrason. Ferroelectr. Freq. Control*, vol. 39, no. 2, pp. 262–7, Jan. 1992, doi: 10.1109/58.139123.

[47] M. L. Palmeri, A. C. Sharma, R. R. Bouchard, R. W. Nightingale, and K. R. Nightingale, "A finite-element method model of soft tissue response to impulsive acoustic radiation force.," *IEEE Trans. Ultrason. Ferroelectr. Freq. Control*, vol. 52, no. 10, pp. 1699–712, Oct. 2005, doi: 10.1109/TUFFC.2005.1561624.

[48] M. L. Palmeri, S. a. McAleavey, G. E. Trahey, and K. R. Nightingale, "Ultrasonic tracking of acoustic radiation force-induced displacements in homogeneous media," *IEEE Trans. Ultrason. Ferroelectr. Freq. Control*, vol. 53, no. 7, pp. 1300–1313, 2006, doi: 10.1109/TUFFC.2006.1665078.

[49] M. M. Hossain and C. M. Gallippi, "Electronic Point Spread Function Rotation Using a Three-Row Transducer for ARFI-Based Elastic Anisotropy Assessment: In Silico and Experimental Demonstration.," *IEEE Trans. Ultrason. Ferroelectr. Freq. Control*, vol. 68, no. 3, pp. 632–646, Mar. 2021, doi: 10.1109/TUFFC.2020.3019002.

[50] G. F. Pinton, J. J. Dahl, and G. E. Trahey, "Rapid tracking of small displacements with ultrasound.," *IEEE Trans. Ultrason. Ferroelectr. Freq. Control*, vol. 53, no. 6, pp. 1103–17, Jun. 2006, doi: 10.1109/ULTSYM.2005.1603285.

[51] M. M. Hossain *et al.*, "Mechanical Anisotropy Assessment in Kidney Cortex Using ARFI Peak Displacement: Preclinical Validation and Pilot In Vivo Clinical Results in Kidney Allografts.," *IEEE Trans. Ultrason. Ferroelectr. Freq. Control*, vol. 66, no. 3, pp. 551–562, Mar. 2019, doi: 10.1109/TUFFC.2018.2865203.

[52] M. M. Hossain *et al.*, "Evaluating Renal Transplant Status Using Viscoelastic Response (VisR) Ultrasound.," *Ultrasound Med. Biol.*, vol. 44, no. 8, pp. 1573–1584, May 2018, doi: 10.1016/j.ultrasmedbio.2018.03.016.

[53] K. A. Skalina, S. Singh, C. G. Chavez, F. Macian, and C. Guha, "Low Intensity Focused Ultrasound (LOFU)-mediated Acoustic Immune Priming and Ablative Radiation Therapy for in situ Tumor Vaccines.," *Sci. Rep.*, vol. 9, no. 1, p. 15516, 2019, doi: 10.1038/s41598-019-51332-4.

[54] T. Savage, S. Pandey, and C. Guha, "Postablation Modulation after Single High-Dose Radiation Therapy Improves Tumor Control via Enhanced Immunomodulation," *Clin. Cancer Res.*, vol. 26, no. 4, pp. 910–921, Feb. 2020, doi: 10.1158/1078-0432.CCR-18-3518.

[55] G. Montaldo, M. Tanter, J. Bercoff, N. Benech, and M. Fink, "Coherent plane-wave compounding for very high frame rate ultrasonography and transient elastography.," *IEEE Trans. Ultrason. Ferroelectr. Freq. Control*, vol. 56, no. 3, pp. 489–506, Mar. 2009, doi: 10.1109/TUFFC.2009.1067.

[56] D. M. Giannantonio, D. M. Dumont, G. E. Trahey, and B. C. Byram, "Comparison of physiological motion filters for in vivo cardiac ARFI.," *Ultrason. Imaging*, vol. 33, no. 2, pp. 89–108, Apr. 2011, doi: 10.1177/016173461103300201.

[57] K. Nightingale, M. Palmeri, and G. Trahey, "Analysis of contrast in images generated with transient acoustic radiation force.," *Ultrasound Med. Biol.*, vol. 32, no. 1, pp. 61–72, Jan. 2006, doi: 10.1016/j.ultrasmedbio.2005.08.008.

[58] N. Saharkhiz *et al.*, "Harmonic motion imaging of human breast masses: an in vivo clinical feasibility.," *Sci. Rep.*, vol. 10, no. 1, p. 15254, Sep. 2020, doi: 10.1038/s41598-020-71960-5.

[59] J. Bercoff, M. Tanter, and M. Fink, "Supersonic shear imaging: a new technique for soft tissue elasticity mapping.," *IEEE Trans. Ultrason. Ferroelectr. Freq. Control*, vol. 51, no. 4, pp. 396–409, Apr. 2004, doi: 10.1109/TUFFC.2004.1295425.

[60] K. Nightingale, S. McAleavey, and G. Trahey, "Shear-wave generation using acoustic radiation force: in vivo and ex vivo results.," *Ultrasound Med. Biol.*, vol. 29, no. 12, pp. 1715–1723, Dec. 2003, doi: 10.1016/j.ultrasmedbio.2003.08.008.

[61] M. W. Urban, S. Chen, and M. Fatemi, "A Review of Shearwave Dispersion Ultrasound Vibrometry (SDUV) and its Applications," *Curr. Med. Imaging Rev.*, vol. 8, no. 1, pp. 27–36, Feb. 2012, doi: 10.2174/157340512799220625.

[62] D. Y. Chan, D. Cody Morris, T. J. Polascik, M. L. Palmeri, and K. R. Nightingale, "Deep Convolutional Neural Networks for Displacement Estimation in ARFI Imaging," *IEEE Trans. Ultrason. Ferroelectr. Freq. Control*, vol. 3010, no. c, pp. 1–1, 2021, doi: 10.1109/TUFFC.2021.3068377.

[63] M. Ashikuzzaman and H. Rivaz, "Second-Order Ultrasound Elastography With L 1-Norm Spatial Regularization," *IEEE Trans. Ultrason. Ferroelectr. Freq. Control*, vol. 69, no. 3, pp. 1008–1019, Mar. 2022, doi: 10.1109/TUFFC.2022.3141686.

[64] R. Al Mukaddim, N. H. Meshram, and T. Varghese, "Locally optimized correlation-guided Bayesian adaptive regularization for ultrasound strain imaging," *Phys. Med. Biol.*, vol. 65, no. 6, p. 065008, Mar. 2020, doi: 10.1088/1361-6560/ab735f.

[65] M. Mirzaei, A. Asif, and H. Rivaz, "Combining Total Variation Regularization with Window-Based Time Delay Estimation in Ultrasound Elastography," *IEEE Trans. Med. Imaging*, vol. 38, no. 12, pp. 2744–2754, Dec. 2019, doi: 10.1109/TMI.2019.2913194.

[66] S. a. McAleavey, K. R. Nightingale, and G. E. Trahey, "Estimates of echo correlation and measurement bias in acoustic radiation force impulse imaging.,"

IEEE Trans. Ultrason. Ferroelectr. Freq. Control, vol. 50, no. 6, pp. 631–41, Jun. 2003, doi: 10.1109/tuffc.2003.1209550.

[67] P. Song, H. Zhao, A. Manduca, M. W. Urban, J. F. Greenleaf, and S. Chen, "Comb-Push Ultrasound Shear Elastography (CUSE): A Novel Method for Two-Dimensional Shear Elasticity Imaging of Soft Tissues," *IEEE Trans. Med. Imaging*, vol. 31, no. 9, pp. 1821–1832, Sep. 2012, doi: 10.1109/TMI.2012.2205586.

[68] T. J. Czernuszewicz *et al.*, "Performance of acoustic radiation force impulse ultrasound imaging for carotid plaque characterization with histologic validation," *J. Vasc. Surg.*, vol. 66, no. 6, pp. 1749-1757.e3, Dec. 2017, doi: 10.1016/j.jvs.2017.04.043.

[69] M. M. Hossain and C. M. Gallippi, "Quantitative Estimation of Mechanical Anisotropy using Acoustic Radiation Force (ARF)-Induced Peak Displacements (PD): In Silico and Experimental Demonstration.," *IEEE Trans. Med. Imaging*, vol. PP, no. X, pp. 1–14, Jan. 2022, doi: 10.1109/TMI.2022.3141084.

[70] J. R. Doherty *et al.*, "Comparison of Acoustic Radiation Force Impulse Imaging Derived Carotid Plaque Stiffness With Spatially Registered MRI Determined Composition.," *IEEE Trans. Med. Imaging*, vol. 34, no. 11, pp. 2354–65, Nov. 2015, doi: 10.1109/TMI.2015.2432797.

[71] D. C. Morris *et al.*, "Multiparametric Ultrasound for Targeting Prostate Cancer: Combining ARFI, SWEI, QUS and B-Mode," *Ultrasound Med. Biol.*, vol. 81, no. 1, pp. e89–e92, Sep. 2020, doi: 10.1016/j.ultrasmedbio.2020.08.022.

[72] K. Skerl, S. Vinnicombe, K. Thomson, D. McLean, E. Giannotti, and A. Evans, "Anisotropy of Solid Breast Lesions in 2D Shear Wave Elastography is an Indicator of Malignancy," *Acad. Radiol.*, vol. 23, no. 1, pp. 53–61, Jan. 2016, doi: 10.1016/j.acra.2015.09.016.

[73] M. Hossain, C. J. Moore, and C. M. Gallippi, "Acoustic Radiation Force Impulse-Induced Peak Displacements Reflect Degree of Anisotropy in Transversely Isotropic Elastic Materials," *IEEE Trans. Ultrason. Ferroelectr. Freq. Control*, vol. 64, no. 6, pp. 989–1001, Jun. 2017, doi: 10.1109/TUFFC.2017.2690223.